Eur. Phys. J. C 12, 567–586 (2000)
Digital Object Identifier (DOI) 10.1007/s100520000286

THE EUROPEAN PHYSICAL JOURNAL C

Search for neutral Higgs bosons in e^+e^- collisions at $\sqrt{s} \approx 189$ GeV

The OPAL Collaboration

G. Abbiendi[2], K. Ackerstaff[8], G. Alexander[23], J. Allison[16], K.J. Anderson[9], S. Anderson[12], S. Arcelli[17], S. Asai[24], S.F. Ashby[1], D. Axen[29], G. Azuelos[18,a], A.H. Ball[8], E. Barberio[8], R.J. Barlow[16], J.R. Batley[5], S. Baumann[3], J. Bechtluft[14], T. Behnke[27], K.W. Bell[20], G. Bella[23], A. Bellerive[9], S. Bentvelsen[8], S. Bethke[14], S. Betts[15], O. Biebel[14], A. Biguzzi[5], I.J. Bloodworth[1], P. Bock[11], J. Böhme[14], O. Boeriu[10], D. Bonacorsi[2], M. Boutemeur[33], S. Braibant[8], P. Bright-Thomas[1], L. Brigliadori[2], R.M. Brown[20], H.J. Burckhart[8], P. Capiluppi[2], R.K. Carnegie[6], A.A. Carter[13], J.R. Carter[5], C.Y. Chang[17], D.G. Charlton[1,b], D. Chrisman[4], C. Ciocca[2], P.E.L. Clarke[15], E. Clay[15], I. Cohen[23], J.E. Conboy[15], O.C. Cooke[8], J. Couchman[15], C. Couyoumtzelis[13], R.L. Coxe[9], M. Cuffiani[2], S. Dado[22], G.M. Dallavalle[2], S. Dallison[16], R. Davis[30], S. De Jong[12], A. de Roeck[8], P. Dervan[15], K. Desch[27], B. Dienes[32,h], M.S. Dixit[7], M. Donkers[6], J. Dubbert[33], E. Duchovni[26], G. Duckeck[33], I.P. Duerdoth[16], P.G. Estabrooks[6], E. Etzion[23], F. Fabbri[2], A. Fanfani[2], M. Fanti[2], A.A. Faust[30], L. Feld[10], P. Ferrari[12], F. Fiedler[27], M. Fierro[2], I. Fleck[10], A. Frey[8], A. Fürtjes[8], D.I. Futyan[16], P. Gagnon[7], J.W. Gary[4], G. Gaycken[27], C. Geich-Gimbel[3], G. Giacomelli[2], P. Giacomelli[2], W.R. Gibson[13], D.M. Gingrich[30,a], D. Glenzinski[9], J. Goldberg[22], W. Gorn[4], C. Grandi[2], K. Graham[28], E. Gross[26], J. Grunhaus[23], M. Gruwé[27], C. Hajdu[31] G.G. Hanson[12], M. Hansroul[8], M. Hapke[13], K. Harder[27], A. Harel[22], C.K. Hargrove[7], M. Harin-Dirac[4], M. Hauschild[8], C.M. Hawkes[1], R. Hawkings[27], R.J. Hemingway[6], G. Herten[10], R.D. Heuer[27], M.D. Hildreth[8], J.C. Hill[5], P.R. Hobson[25], A. Hocker[9], K. Hoffman[8], R.J. Homer[1], A.K. Honma[28,a], D. Horváth[31,c], K.R. Hossain[30], R. Howard[29], P. Hüntemeyer[27], P. Igo-Kemenes[11], D.C. Imrie[25], K. Ishii[24], F.R. Jacob[20], A. Jawahery[17], H. Jeremie[18], M. Jimack[1], C.R. Jones[5], P. Jovanovic[1], T.R. Junk[6], N. Kanaya[24], J. Kanzaki[24], D. Karlen[6], V. Kartvelishvili[16], K. Kawagoe[24], T. Kawamoto[24], P.I. Kayal[30], R.K. Keeler[28], R.G. Kellogg[17], B.W. Kennedy[20], D.H. Kim[19], A. Klier[26], T. Kobayashi[24], M. Kobel[3,d], T.P. Kokott[3], M. Kolrep[10], S. Komamiya[24], R.V. Kowalewski[28], T. Kress[4], P. Krieger[6], J. von Krogh[11], T. Kuhl[3], P. Kyberd[13], G.D. Lafferty[16], H. Landsman[22], D. Lanske[14], J. Lauber[15], I. Lawson[28], J.G. Layter[4], D. Lellouch[26], J. Letts[12], L. Levinson[26], R. Liebisch[11], J. Lillich[10], B. List[8], C. Littlewood[5], A.W. Lloyd[1], S.L. Lloyd[13], F.K. Loebinger[16], G.D. Long[28], M.J. Losty[7], J. Lu[29], J. Ludwig[10], D. Liu[12], A. Macchiolo[18], A. Macpherson[30], W. Mader[3], M. Mannelli[8], S. Marcellini[2], T.E. Marchant[16], A.J. Martin[13], J.P. Martin[18], G. Martinez[17], T. Mashimo[24], P. Mättig[26], W.J. McDonald[30], J. McKenna[29], E.A. Mckigney[15], T.J. McMahon[1], R.A. McPherson[28], F. Meijers[8], P. Mendez-Lorenzo[33], F.S. Merritt[9], H. Mes[7], I. Meyer[5], A. Michelini[2], S. Mihara[24], G. Mikenberg[26], D.J. Miller[15], W. Mohr[10], A. Montanari[2], T. Mori[24], K. Nagai[8], I. Nakamura[24], H.A. Neal[12,g], R. Nisius[8], S.W. O'Neale[1], F.G. Oakham[7], F. Odorici[2], H.O. Ogren[12], A. Okpara[11], M.J. Oreglia[9], S. Orito[24], G. Pásztor[31], J.R. Pater[16], G.N. Patrick[20], J. Patt[10], R. Perez-Ochoa[8], S. Petzold[27], P. Pfeifenschneider[14], J.E. Pilcher[9], J. Pinfold[30], D.E. Plane[8], P. Poffenberger[28], B. Poli[2], J. Polok[8], M. Przybycień[8,e], A. Quadt[8], C. Rembser[8], H. Rick[8], S. Robertson[28], S.A. Robins[22], N. Rodning[30], J.M. Roney[28], S. Rosati[3], K. Roscoe[16], A.M. Rossi[2], Y. Rozen[22], K. Runge[10], O. Runolfsson[8], D.R. Rust[12], K. Sachs[10], T. Saeki[24], O. Sahr[33], W.M. Sang[25], E.K.G. Sarkisyan[23], C. Sbarra[29], A.D. Schaile[33], O. Schaile[33], P. Scharff-Hansen[8], J. Schieck[11], S. Schmitt[11], A. Schöning[8], M. Schröder[8], M. Schumacher[3], C. Schwick[8], W.G. Scott[20], R. Seuster[14], T.G. Shears[8], B.C. Shen[4], C.H. Shepherd-Themistocleous[5], P. Sherwood[15], G.P. Siroli[2], A. Skuja[17], A.M. Smith[8], G.A. Snow[17], R. Sobie[28], S. Söldner-Rembold[10,f], S. Spagnolo[20], M. Sproston[20], A. Stahl[3], K. Stephens[16], K. Stoll[10], D. Strom[19], R. Ströhmer[33], B. Surrow[8], S.D. Talbot[1], P. Taras[18], S. Tarem[22], R. Teuscher[9], M. Thiergen[10], J. Thomas[15], M.A. Thomson[8], E. Torrence[8], S. Towers[6], T. Trefzger[33], I. Trigger[18], Z. Trócsányi[32,h], E. Tsur[23], M.F. Turner-Watson[1], I. Ueda[24], R. Van Kooten[12], P. Vannerem[10], M. Verzocchi[8], H. Voss[3], F. Wäckerle[10], A. Wagner[27], D. Waller[6], C.P. Ward[5], D.R. Ward[5], P.M. Watkins[1], A.T. Watson[1], N.K. Watson[1], P.S. Wells[8], N. Wermes[3], D. Wetterling[11] J.S. White[6], G.W. Wilson[16], J.A. Wilson[1], T.R. Wyatt[16], S. Yamashita[24], V. Zacek[18], D. Zer-Zion[8]

[1] School of Physics and Astronomy, University of Birmingham, Birmingham B15 2TT, UK
[2] Dipartimento di Fisica dell' Università di Bologna and INFN, 40126 Bologna, Italy
[3] Physikalisches Institut, Universität Bonn, 53115 Bonn, Germany
[4] Department of Physics, University of California, Riverside CA 92521, USA
[5] Cavendish Laboratory, Cambridge CB3 0HE, UK
[6] Ottawa-Carleton Institute for Physics, Department of Physics, Carleton University, Ottawa, Ontario K1S 5B6, Canada
[7] Centre for Research in Particle Physics, Carleton University, Ottawa, Ontario K1S 5B6, Canada

[8] CERN, European Organisation for Particle Physics, 1211 Geneva 23, Switzerland
[9] Enrico Fermi Institute and Department of Physics, University of Chicago, Chicago IL 60637, USA
[10] Fakultät für Physik, Albert Ludwigs Universität, 79104 Freiburg, Germany
[11] Physikalisches Institut, Universität Heidelberg, 69120 Heidelberg, Germany
[12] Indiana University, Department of Physics, Swain Hall West 117, Bloomington IN 47405, USA
[13] Queen Mary and Westfield College, University of London, London E1 4NS, UK
[14] Technische Hochschule Aachen, III Physikalisches Institut, Sommerfeldstrasse 26-28, 52056 Aachen, Germany
[15] University College London, London WC1E 6BT, UK
[16] Department of Physics, Schuster Laboratory, The University, Manchester M13 9PL, UK
[17] Department of Physics, University of Maryland, College Park, MD 20742, USA
[18] Laboratoire de Physique Nucléaire, Université de Montréal, Montréal, Quebec H3C 3J7, Canada
[19] University of Oregon, Department of Physics, Eugene OR 97403, USA
[20] CLRC Rutherford Appleton Laboratory, Chilton, Didcot, Oxfordshire OX11 0QX, UK
[21] Department of Physics, Technion-Israel Institute of Technology, Haifa 32000, Israel
[22] Department of Physics and Astronomy, Tel Aviv University, Tel Aviv 69978, Israel
[23] International Centre for Elementary Particle Physics and Department of Physics, University of Tokyo, Tokyo 113-0033, and Kobe University, Kobe 657-8501, Japan
[24] Institute of Physical and Environmental Sciences, Brunel University, Uxbridge, Middlesex UB8 3PH, UK
[25] Particle Physics Department, Weizmann Institute of Science, Rehovot 76100, Israel
[26] Universität Hamburg/DESY, II Institut für Experimental Physik, Notkestrasse 85, 22607 Hamburg, Germany
[27] University of Victoria, Department of Physics, P O Box 3055, Victoria BC V8W 3P6, Canada
[28] University of British Columbia, Department of Physics, Vancouver BC V6T 1Z1, Canada
[29] University of Alberta, Department of Physics, Edmonton AB T6G 2J1, Canada
[30] Research Institute for Particle and Nuclear Physics, 1525 Budapest, P O Box 49, Hungary
[31] Institute of Nuclear Research, 4001 Debrecen, P O Box 51, Hungary
[32] Ludwigs-Maximilians-Universität München, Sektion Physik, Am Coulombwall 1, 85748 Garching, Germany

Received: 9 July 1999 / Published online: 27 January 2000 –

Abstract. Searches for the neutral Higgs bosons predicted by the Standard Model (SM) and the Minimal Supersymmetric extension of the Standard Model (MSSM) have been performed with the OPAL detector at LEP. Approximately $170\,\mathrm{pb}^{-1}$ of e^+e^- collision data collected at $\sqrt{s} \approx 189\,\mathrm{GeV}$ were used to search for Higgs boson production in the SM process $e^+e^- \to H^0Z^0$ and the MSSM processes $e^+e^- \to h^0Z^0$ and $e^+e^- \to A^0h^0$. The searches are sensitive to the $b\bar{b}$ and $\tau^+\tau^-$ decay modes of the Higgs bosons, and also to the MSSM decay mode $h^0 \to A^0A^0$. OPAL search results at lower centre-of-mass energies have been incorporated in the limits, which are valid at the 95% confidence level. For the SM Higgs boson, a lower mass bound of 91.0 GeV is obtained. In the MSSM, the limits are $m_H > 74.8\,\mathrm{GeV}$ and $m_A > 76.5\,\mathrm{GeV}$, assuming $\tan\beta > 1$, that the mixing of the scalar top quarks is either zero or maximal, and that the soft SUSY-breaking masses are 1 TeV. For the case of zero scalar top mixing, the values of $\tan\beta$ between 0.72 and 2.19 are excluded.

1 Introduction

The OPAL detector at LEP has collected more than $185\,\mathrm{pb}^{-1}$ of e^+e^- collision data at centre-of-mass energies in the vicinity of 189 GeV. These data are used to search for neutral Higgs bosons [1] within the framework of the Standard Model (SM) [2], and within the Minimal Supersymmetric extension of the Standard Model (MSSM) [3]. Searches have been performed for the "Higgs-strahlung" process, $e^+e^- \to h^0Z^0 \to h^0 f\bar{f}$, where h^0 is either the SM Higgs boson H^0_{SM} or the lightest neutral CP-even Higgs boson in the MSSM, and $f\bar{f}$ is a fermion-antifermion pair from Z^0 decay. For the $h^0\nu\bar{\nu}$ ($h^0e^+e^-$) final state, the contribution from the WW (ZZ) fusion process is also taken into account. Searches have also been performed for the MSSM process $e^+e^- \to A^0h^0$, where A^0 is the CP-odd Higgs boson.

In this paper, only the dominant decays of the neutral Higgs bosons (h^0 and A^0) into $b\bar{b}$ pairs and $\tau^+\tau^-$ pairs are considered. The sensitivities of the searches to the MSSM decay sequence $h^0 \to A^0A^0$ with $A^0 \to b\bar{b}$ are also considered. Searches for Higgs boson decays into SUSY particles are not presented in this paper. OPAL searches for Higgs boson production in data taken at centre-of-mass energies up to 184 GeV have been reported in [4–6] for the neutral Higgs bosons of the SM and the MSSM. For the SM Higgs boson a lower mass bound of $m_h > 88.3\,\mathrm{GeV}$ was obtained at the 95% confidence level from the lower-

[a] and at TRIUMF, Vancouver, Canada V6T 2A3
[b] and Royal Society University Research Fellow
[c] and Institute of Nuclear Research, Debrecen, Hungary
[d] on leave of absence from the University of Freiburg
[e] and University of Mining and Metallurgy, Cracow
[f] and Heisenberg Fellow
[g] now at Yale University, Department of Physics, New Haven, USA
[h] and Department of Experimental Physics, Lajos Kossuth University, Debrecen, Hungary

energy searches. The searches presented here are similar in procedure to OPAL's previous searches at $\sqrt{s} \approx 183\,\mathrm{GeV}$ [4]; in this paper only significant changes from the previous analyses are described in detail. In particular, the b-tagging algorithm has been significantly improved; the new algorithm is described in detail in Sect. 3.

The selection requirements in each of the searches are optimised to maximise the sensitivity to Higgs boson production. In each case, the mass limit one would expect to set in the absence of a Higgs boson signal, computed using Monte Carlo simulations of signal and background processes, is maximised. When the distribution of a variable in the signal Monte Carlo is needed as an input to a selection technique, a mixture of signal Monte Carlo samples is used with Higgs boson masses near the expected limit in order to optimise the analyses over the range of masses under study.

Recent searches for neutral Higgs particles performed by the other LEP collaborations are listed in [7]. The combined mass limit by the four LEP collaborations for the SM Higgs boson and a combination of the MSSM Higgs boson searches using data taken at $\sqrt{s} \leq 184\,\mathrm{GeV}$ are reported in [8].

2 OPAL detector, data sets and Monte Carlo samples

The present analysis is based on data collected with the OPAL detector [9] during 1998 at a luminosity-weighted average centre-of-mass energy of 188.6 GeV. The searches presented here use subsets of the data sample for which the necessary detector components were fully operational. Approximately 170 pb^{-1} were analysed, varying $\pm 2\%$ from channel to channel, depending on the subdetectors required. In addition, approximately 3.1 pb^{-1} of data were collected at $\sqrt{s} \approx m_{\mathrm{Z}^0}$ to provide detector calibration and to test Monte Carlo simulations.

The solid angle coverage of the OPAL detector is nearly complete. The central tracking detector consists of a high-resolution silicon microstrip vertex detector [10] which immediately surrounds the beam pipe. Its coverage in polar angle[1] is $|\cos\theta| < 0.9$. The silicon microvertex detector is followed by a high-precision vertex drift chamber, a large-volume jet chamber, and z–chambers to measure the z coordinate of tracks, all in a uniform 0.435 T axial magnetic field. The lead-glass electromagnetic calorimeter with a presampler is located outside the magnet coil. It provides, in combination with the forward calorimeters, the forward scintillating tile counter (the "MIP plug") [11], and the silicon-tungsten luminometer [12], geometrical acceptance down to 25 mrad from the beam direction. The silicon-tungsten luminometer serves to measure the integrated luminosity using small-angle Bhabha scattering events [13]. The magnet return yoke is instrumented with streamer tubes and thin gap chambers for hadron calorimetry; it is surrounded by several layers of muon chambers.

Events are reconstructed from charged particle tracks and energy deposits ("clusters") in the electromagnetic and hadron calorimeters. The tracks and clusters must pass a set of quality requirements similar to those used in [14]. The selection procedures described in this paper make use of the Durham algorithm [15] to group the reconstructed tracks and clusters into jets. The details of the resolutions used and whether the association of tracks and clusters to jets is adjusted from the Durham algorithm's result depend on the search channel. In calculating the total visible energies and momenta, E_{vis} and $\mathbf{P}_{\mathrm{vis}}$, of events and of individual jets, "energy-flow objects" are formed from the tracks and calorimeter clusters [16]. The energies expected to be deposited in the calorimeters by the charged particles measured in the tracking chambers are subtracted from the energies of their associated calorimeter clusters. The tracks and the remaining clusters are taken to be the energy-flow objects. This procedure provides the best estimates of the energies of particles which leave signals in more than one subdetector.

The detection efficiencies for Higgs boson production and the selection rates for SM background processes have been estimated using a variety of Monte Carlo models. Higgs boson production is modelled with the HZHA generator [17] for a wide range of Higgs boson masses. The size of these samples varies from 500 to 10,000 events. The background processes are simulated with typically more than 50 times the statistics of the collected data. The following event generators are used: PYTHIA [18] ($(\mathrm{Z}/\gamma)^* \to \mathrm{q\bar{q}}(\gamma)$), grc4f [19] and EXCALIBUR [20] (four-fermion processes (4f)), BHWIDE [21] ($\mathrm{e^+e^-}(\gamma)$), KORALZ [22] ($\mu^+\mu^-(\gamma)$ and $\tau^+\tau^-(\gamma)$), and PHOJET [23], HERWIG [24] and Vermaseren [25] (hadronic and leptonic two-photon processes ($\gamma\gamma$)). The hadronisation process is simulated with JETSET [18] with parameters described in [26]. The cluster fragmentation model in HERWIG is used to study the uncertainties due to fragmentation and hadronisation. For each Monte Carlo sample, the detector response to the generated particles is simulated in full detail [27].

3 Improved b-tagging

The predominant decay mode of the SM Higgs boson in the mass range under study is expected to be to pairs of b quarks; the same is true of the neutral Higgs bosons of the MSSM for many choices of values for the MSSM parameters. Therefore, efficient and pure tagging of b quarks is essential in searches for these particles. A tagging method [4] has been developed which uses the three nearly independent techniques of lifetime, high-p_t lepton and kinematic tagging to identify jets containing b hadron decays and to minimise the contamination from jets which do not. Artificial Neural Networks (ANN's) have been introduced to

[1] OPAL uses a right-handed coordinate system where the $+z$ direction is along the electron beam and where $+x$ points to the centre of the LEP ring. The polar angle θ is defined with respect to the $+z$ direction and the azimuthal angle ϕ with respect to the $+x$ direction.

combine optimally several lifetime-sensitive tagging variables and also to combine kinematic variables in the jet-kinematics part of the tag. For each jet, the outputs of the lifetime ANN, the kinematic ANN and the lepton tag are combined into a likelihood variable $\mathcal{B}$ which discriminates b-flavoured jets from c-flavoured and uds-flavoured jets. While the basic scheme of the tagging procedure has been kept unchanged with respect to OPAL's previous procedure [4], a significant improvement in the performance has been achieved for this analysis by introducing input variables with greater sensitivity.

In order to improve the performance of the lifetime-sensitive part of the tag, a new algorithm has been developed to identify displaced vertices. An ANN applied to individual tracks (track-ANN) has been trained to discriminate between tracks from the primary vertex and those from secondary vertices. The training procedure uses Monte Carlo samples simulating the process $e^+e^- \to Z^0 \to$hadrons at $\sqrt{s} \approx m_{Z^0}$. The track-ANN uses, among other inputs, the impact parameter of the track with respect to the primary vertex and the transverse momentum with respect to the jet axis. The jet axis is defined to be the direction of the sum of the momenta of the energy-flow objects belonging to the jet. The tracks belonging to a given jet are ranked in descending order of their probability of having come from a secondary vertex, according to the track-ANN output. Using the first six tracks (or all tracks in the jet if there are fewer than six), a "seed" vertex is formed using the technique described in [28]. Following this technique, a vertex is first formed from the input tracks, and then the track which contributes the most to the vertex χ^2 is removed. This procedure is repeated until no track contributes more than 5 to the χ^2. The seed vertex is the common fit origin of the tracks. The remaining tracks in the jet are then tested to see if they may be added to the seed vertex, based on their contributions to the vertex χ^2.

In addition to identifying displaced vertices, a combination of the significances of the track impact parameters in the event is used in order to gain b-tagging efficiency in events where the secondary vertices are less distinct. In this method, the impact parameter significances $S^{r\phi}$ and S^{rz}, in the $r\phi$ and rz projections, respectively, are formed by dividing the track impact parameters by their estimated errors. The distributions of $S^{r\phi}$ and S^{rz} for each quark flavour from the $Z^0 \to$hadrons Monte Carlo are used as the probability density functions (PDF's) $f_q^{r\phi}$ and f_q^{rz} (q=uds, c and b). The combined estimator F_q for each quark flavour q is computed by multiplying the $f_q^{r\phi}$ and f_q^{rz} for all tracks passing the quality requirements. The final estimator $\mathcal{L}_{\mathrm{IP}}$ is obtained as the ratio of F_b to the sum of F_{uds}, F_c and F_b.

The following four variables are used as inputs to the lifetime ANN. They replace the five variables used in our 183 GeV analysis [4].

- The vertex significance likelihood ($\mathcal{L}_{\mathrm{V}}$): The likelihood for the vertex significance is computed analogously to the $\mathcal{L}_{\mathrm{IP}}$ above, using the decay length significance of the secondary vertex rather than the impact parameter significance of the tracks. Because the decay length significance of a secondary vertex depends strongly on the number of tracks in it, the PDF's for each flavour are computed separately for each value of the number of tracks assigned to the secondary vertex.
- The reduced significance likelihood ($\mathcal{R}_{\mathrm{V}}$): To reduce sensitivity to single mismeasured tracks, the track with the largest impact parameter significance with respect to the primary vertex is removed from the secondary vertex candidate and the remaining tracks are used to recompute the likelihood $\mathcal{L}_{\mathrm{V}}$. If the original vertex has only two tracks, the function is calculated from the impact parameter significance of the remaining track.
- The combined impact parameter likelihood ($\mathcal{L}_{\mathrm{IP}}$) described above.
- The reduced impact parameter likelihood ($\mathcal{R}_{\mathrm{IP}}$): The track having the largest impact parameter significance has been removed in the calculation of $\mathcal{L}_{\mathrm{IP}}$.

In the jet-kinematics part of the tag, the procedure employed at $\sqrt{s} \approx 183\,\mathrm{GeV}$ used only the boosted sphericity of the jet as an input to the final likelihood. The boosted sphericity is defined to be the sphericity [29] of the jet computed in its rest frame. The sphericity axis is the direction of the eigenvector of the sphericity tensor with the largest eigenvalue. This boosted sphericity has been replaced with three new variables, which are combined with a separate ANN. These three inputs are 1) the number of energy-flow objects within 0.4 radians of the jet axis, 2) the angle between the jet axis and the jet sphericity axis in the rest frame of the jet, and 3) the C-parameter [30] of the jet in its rest frame. The high-p_t lepton tag has not been changed.

The outputs from the lifetime ANN, the jet-kinematics ANN and the high-p_t lepton tag are combined with an unbinned likelihood calculation as described in [4], and the final output $\mathcal{B}$ is computed for each jet. Figure 1a shows the distribution of $\mathcal{B}$ for data taken at $\sqrt{s} \approx m_{Z^0}$ in 1998; it also shows the improved performance of the new b-tagging algorithm, compared with the previous version [4]. For the same efficiency, the new b-tag has about two thirds of the background acceptance of the previous tag. The tagging efficiency for b-flavoured jets has been verified to an accuracy of 1% with a double tagging technique using the data collected at $\sqrt{s} \approx m_{Z^0}$ with the same detector configuration and operating conditions as the high-energy data; a comparison of the results of this double tagging test between the data and Monte Carlo is shown in Fig. 1b. The b-tag fraction in the high-energy data and the b-tag fraction in corresponding Standard Model Monte Carlo samples agree within a relative statistical uncertainty of 5% for samples enriched in $(Z/\gamma)^* \to q\bar{q}$ processes with and without hard initial-state photon radiation. For the lighter flavours, the tag fraction has been examined by vetoing b flavour in the opposite hemisphere, and the resulting tag rate is found to be described by the Monte Carlo within 5–10%. This uncertainty in the tag rate of light flavours is one component of the systematic uncertainty in the background estimates of the search channels presented in this paper. The efficiency for tagging lighter flavours has also

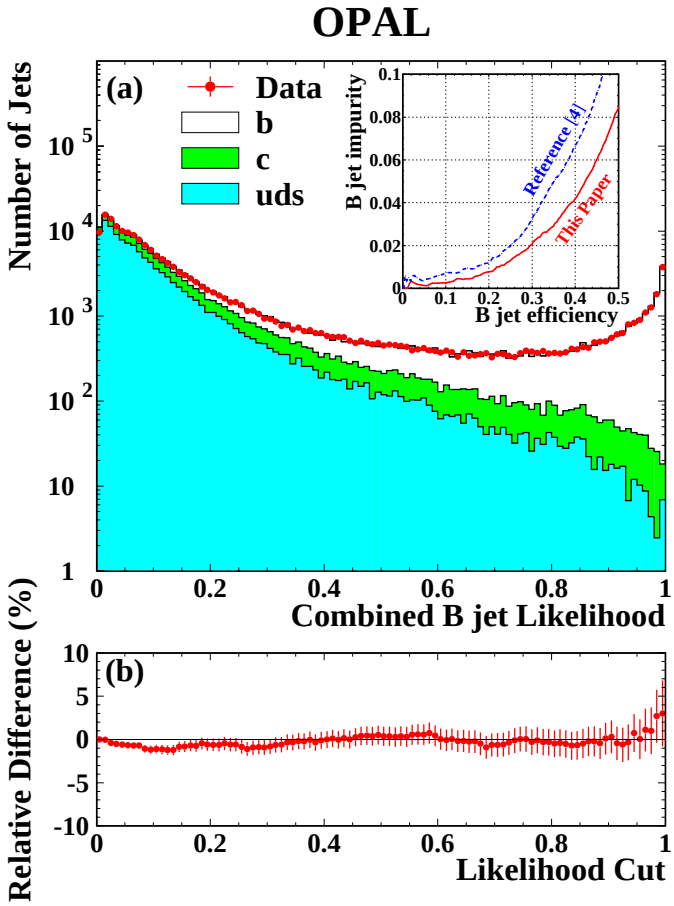

Fig. 1a,b. B-tagging performance and modelling. **a**: the distribution of the output of the b-tagging algorithm, $\mathcal{B}$, for jets in data taken at $\sqrt{s} = m_{\mathrm{Z}^0}$, compared to the Monte Carlo expectation. The data distribution is given by the points, with error bars smaller than the plot symbols. The open histogram shows the distribution of $\mathcal{B}$ for b-flavoured jets, and the dark (light) grey histogram shows the contribution from c (uds) flavoured jets, expected in a Monte Carlo simulation. Inset: The b-tagging performance in the present work for hadronic jets in Z^0 decay compared with our previous version [4]. **b**: the relative difference of the tagging rates for jets opposite to b-tagged jets in Z^0 data and Monte Carlo as a function of the likelihood cut. The points are statistically correlated because the tagging rate accumulates events on one side of the likelihood cut.

been checked by computing $\mathcal{B}$ for a high-purity sample of light-flavour jets in $\mathrm{W}^+\mathrm{W}^- \to q\bar{q}\ell\bar{\nu}$ decays; there is no evidence of mismodelling of the light-flavour tag rate within the statistical precision of the test.

4 Searches for $e^+e^- \to h^0Z^0$

Throughout this section, h^0 denotes both the Standard Model Higgs boson $\mathrm{H}^0_{\mathrm{SM}}$ and the lightest CP-even Higgs boson in the MSSM. Searches are presented for the process $\mathrm{e}^+\mathrm{e}^- \to \mathrm{h}^0\mathrm{Z}^0$ in the following final states: $\mathrm{h}^0\mathrm{Z}^0 \to \mathrm{b\bar{b}q\bar{q}}$ (the four-jet channel), $\mathrm{h}^0\mathrm{Z}^0 \to \mathrm{b\bar{b}}\nu\bar{\nu}$ (the missing-energy channel), $\mathrm{h}^0\mathrm{Z}^0 \to \mathrm{b\bar{b}}\tau^+\tau^-$ and $\tau^+\tau^-\mathrm{q\bar{q}}$ (the tau channels), $\mathrm{h}^0\mathrm{Z}^0 \to \mathrm{b\bar{b}e}^+\mathrm{e}^-$ and $\mathrm{b\bar{b}}\mu^+\mu^-$ (the electron and muon channels). The selections for all channels are similar to those described in [4]; their main features and differences from our previous publication are described in Sects. 4.1 through 4.4. These selections are also sensitive to the $\mathrm{h}^0\mathrm{Z}^0 \to \mathrm{A}^0\mathrm{A}^0\mathrm{Z}^0$ processes of the MSSM, and the procedure for incorporating this additional information into the limits is described in Sect. 4.5.

4.1 The four-jet channel

The selection for the four-jet channel is a modified version of the selection used at $\sqrt{s} \approx 183\,\mathrm{GeV}$. The modifications have been made in order to increase the sensitivity to Higgs boson signals at higher masses. The improved b-tagging algorithm described above is used, and the grouping of final-state particles into four jets and the assignment of pairs of these jets to the Z^0 and h^0 bosons are improved.

The correct assignment of particles to jets plays an essential role in reducing one of the main backgrounds, $\mathrm{W}^+\mathrm{W}^- \to \mathrm{q\bar{q}q\bar{q}}$, and also in accurately reconstructing the Higgs boson mass. The Durham algorithm [15] is used to find four jets in each event, *i.e.*, the resolution parameter y_{cut} is chosen to be between y_{34} and y_{45}, where y_{34} is the transition point from three to four jets, and y_{45} is the transition point from four to five jets. These jets are used as reference jets in the following procedure. Each particle is reassociated to the jet having the smallest "distance" in the E0 scheme [31] of the JADE algorithm [32] to the particle. This "distance" is defined to be $E^i_{jet} \cdot E_{particle} \cdot (1 - \cos\theta_i)$, where E^i_{jet} is the energy of the i^{th} reference jet (i=1 to 4), $E_{particle}$ is the energy of the energy-flow object and θ_i is the angle between the i^{th} reference jet and the particle. This reassociation procedure reduces the fraction of wrong association of particles to jets, which improves by about 10% the di-jet mass resolution for the $\mathrm{W}^+\mathrm{W}^-$ background as well as for Monte Carlo Higgs boson signals, before kinematic fitting. The rearranged jets are used in cuts 5 and 6 of the preselection and the final likelihood selection described below. This procedure is also used for the four-jet $\mathrm{A}^0\mathrm{h}^0$ channel described in Sect. 5.1.

The preselection is the same as that used in [4]; it is designed to retain only four-jet-like events. The requirements are:

1. Events must satisfy the hadronic final state requirement of [33].
2. The effective centre-of-mass energy $\sqrt{s'}$ [33] must be at least 150 GeV.
3. The value of y_{34} in the Durham algorithm must exceed 0.003.
4. The event shape C–parameter [30] must be larger than 0.25.
5. Each of the four jets must have at least two tracks.
6. The χ^2 probabilities must be larger than 10^{-5} both for a four-constraint (4C) kinematic fit, which requires

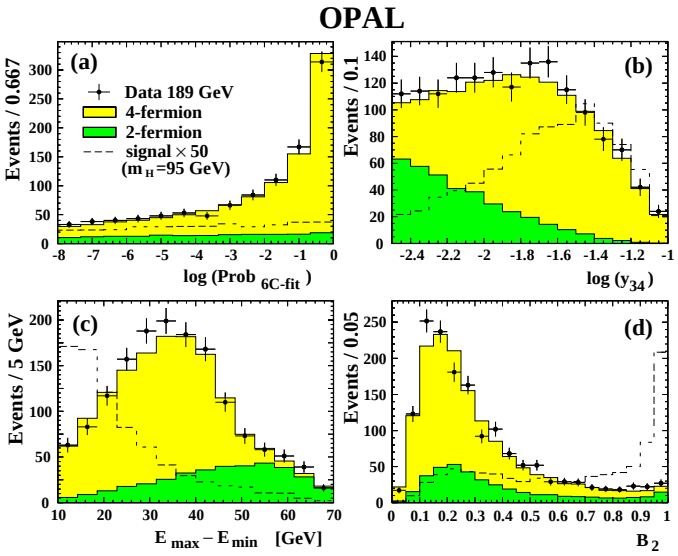

Fig. 2a–d. Input variables for the four-jet channel likelihood selection: **a** the fit probability of a 6C kinematic fit which requires energy and momentum conservation and both dijet masses to be equal to m_{W}; **b** the logarithm of the jet resolution parameter y_{34}; **c** the difference between the energies of the jets with the highest and lowest energies; **d** the second largest jet b-tag. OPAL data are indicated by points with error bars, four-fermion backgrounds by the light grey histograms, and two-fermion backgrounds by the dark grey histograms. The estimated contribution from a 95 GeV Higgs boson is shown with dashed histograms; it has been scaled by a factor of 50.

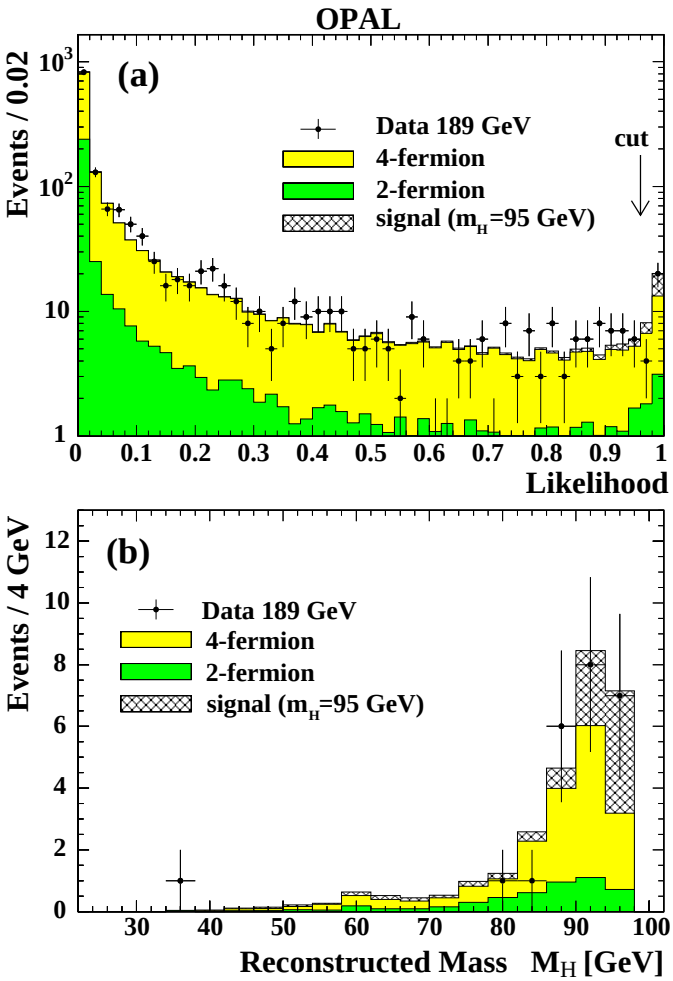

Fig. 3a,b. Four-jet channel: the likelihood distribution **a** and the reconstructed candidate masses **b**. OPAL data are indicated by points with error bars, four-fermion backgrounds by the light grey histograms, and two-fermion backgrounds by the dark grey histograms. Also shown is the contribution expected from a 95 GeV Higgs boson (hatched histograms).

energy and momentum conservation, and a five-constraint (5C) kinematic fit, additionally constraining the invariant mass of one pair of jets to m_{Z^0} [5]. The algorithm used to select the jet pair which is constrained to the Z^0 mass is described below.

There are six possible ways to assign four jets in pairs to the Z^0 and the h^0. An algorithm based on a likelihood technique has been developed in order to select the most Higgs-like combination. This algorithm makes use of b-tagging variables and the probability $p_{5\mathrm{C}}$ for the 5C kinematic fit to have the observed χ^2 or larger. For each of the six jet-assignment combinations, two variables are formed from the b-tagging output as follows: (1) $\mathcal{B}_1 \cdot \mathcal{B}_2$ for jets assigned to the Higgs boson, and (2) $(1-\mathcal{B}_3)\cdot(1-\mathcal{B}_4)$ for jets assigned to the Z^0. These two variables, together with $\log(p_{5\mathrm{C}})$ for the jet combination, are used as inputs to the likelihood calculation, which is designed to distinguish between the following three cases: correct jet assignment, swapped pairings in which the two jets from the h^0 are wrongly assigned to the Z^0, and other combinations, for which one jet from the h^0 is assigned to the Z^0. For each of the possible assignments of pairs of jets to the Z^0 and the h^0 with $p_{5\mathrm{C}} > 10^{-5}$, three likelihoods, $\mathcal{L}^{correct}$, $\mathcal{L}^{swapped}$ and $\mathcal{L}^{others}$, are calculated using the PDF's of the input variables in signal Monte Carlo events passing the preselection. The relative likelihood $\mathcal{L} = \mathcal{L}^{correct} / \left(\mathcal{L}^{correct} + \mathcal{L}^{swapped} + \mathcal{L}^{others}\right)$ is then formed for each combination and the combination yielding the largest value of $\mathcal{L}$ is chosen. The reconstructed Higgs boson mass is taken to be the mass obtained from the 5C kinematic fit for this combination.

With this algorithm, the rate of correct jet pairings for selected signal events with $m_{\mathrm{h}} = 95$ GeV is 71%, compared to the rate of 36% obtained with the method used in our 183 GeV analysis, which uses only $p_{5\mathrm{C}}$ for the assignment. This improvement in the correct jet-pairing reduces the fraction of combinations for which the reconstructed h^0 and Z^0 masses have been swapped. The fraction of signal Monte Carlo events with $m_{\mathrm{h}} = 95\,\mathrm{GeV}$ for which the reconstructed Higgs boson mass is in the Gaussian core centered on 95 GeV increases by 10% when this improved jet pairing is used, as compared to the previous pairing. The correct jet pairing provides better assignment of the b-tag variables to the Higgs boson candidate and improves the separation of the $\mathrm{h}^0\mathrm{Z}^0$ signal from $\mathrm{Z}^0\mathrm{Z}^0$ background.

After the preselection, the eight variables described in [4] are combined using a likelihood method [5]. The distri-

Table 1. The h^0Z^0 channels: the numbers of events after each cut for the data and the expected background, normalised to the data luminosity. The two-photon background, not shown separately, is included in the total background. The last column shows the detection efficiencies, for $h^0 \to b\bar{b}$ in the four-jet channel, for $h^0 \to$ all in the missing-energy, electron, and muon channels, and for $Z^0h^0 \to \tau^+\tau^-(h^0 \to$ all) or $Z^0h^0 \to q\bar{q}\tau^+\tau^-$ in the tau channel, for a Higgs boson mass of 95 GeV with Standard Model branching fractions.

Cut	Data	Total background	$q\bar{q}(\gamma)$ background	four-fermion background	Efficiency (%) $m_h = 95\,\mathrm{GeV}$
		Four-jet Channel	172.1 pb^{-1}		
(1)	18701	18120	14716	3200	99.9
(2)	6242	6183	4215	1954	95.6
(3)	1955	1891	538	1353	91.2
(4)	1927	1864	513	1351	90.1
(5)	1729	1668	436	1231	89.8
(6)	1555	1506	378	1128	88.4
$\mathcal{L}^{HZ}$	24	19.9	4.9	15.0	47.0
		Missing-energy Channel	171.4 pb^{-1}		
(1)	4267	4252	3201	1029	77.9
(2)	1032	1062	341	717	74.1
(3)	981	1016	328	684	73.1
(4)	650	684	56	628	62.4
(5)	184	175	21	154	59.2
(6)	111	101	18	83	57.4
$\mathcal{L}^{HZ}$	10	6.9	1.1	5.7	35.4
		Tau Channel	168.7 pb^{-1}		
Pre-sel	4652	4584	2809	1767	80.4
$\mathcal{L}_{\tau\tau}$	733	693	100	590	62.3
2C fit	201	160	56	104	50.3
1-prong E sum	185	156	55	101	50.0
Final $\mathcal{L}$	3	4.0	0.1	3.9	34.3
		Electron Channel	172.1 pb^{-1}		
(1)	8371	8587	6219	2367	91.0
(2)	521	508	405	102	86.4
(3)	152	153	84	69	75.5
$\mathcal{L}^{HZ}$	3	2.6	0.7	1.9	55.0
		Muon Channel	169.4 pb^{-1}		
(1)	8232	8452	6122	2330	91.0
(2)	103	100	71	29	78.2
(3)	22	22	14	8	75.9
$\mathcal{L}^{HZ}$	1	2.1	0.1	2.0	64.9

butions of four of these variables are shown in Fig. 2 for the OPAL data and corresponding SM background simulations. The likelihood distribution $\mathcal{L}^{HZ}$ and the distribution of the reconstructed Higgs boson candidate masses are shown in Fig. 3. Events are required to have $\mathcal{L}^{HZ} > 0.96$ to be selected as candidates. The numbers of observed and expected events after each selection step are given in Table 1.

After the likelihood selection, 24 candidate events are retained. The expected SM background is 19.9 ± 0.8(stat.) $\pm$ 2.9(syst.) events, computed using Monte Carlo simulations. Within the contribution from $Z^0Z^0 \to q\bar{q}q\bar{q}$ (10.4 events), more than 90% contain at least one Z^0 which decays into $b\bar{b}$. The efficiency for $m_h = 95$ GeV is $(47.0 \pm 0.8(\mathrm{stat.}) \pm 1.6(\mathrm{syst.}))\%$. The systematic errors for the signal selection efficiencies and the background estimates are assigned in the same way as described in [4]. The signal selection efficiency as a function of the h^0 mass is given in Table 4, which summarises the performance of all the SM channels.

In order to verify the correct modelling of the b-tag algorithm in the high-multiplicity four-jet environment,

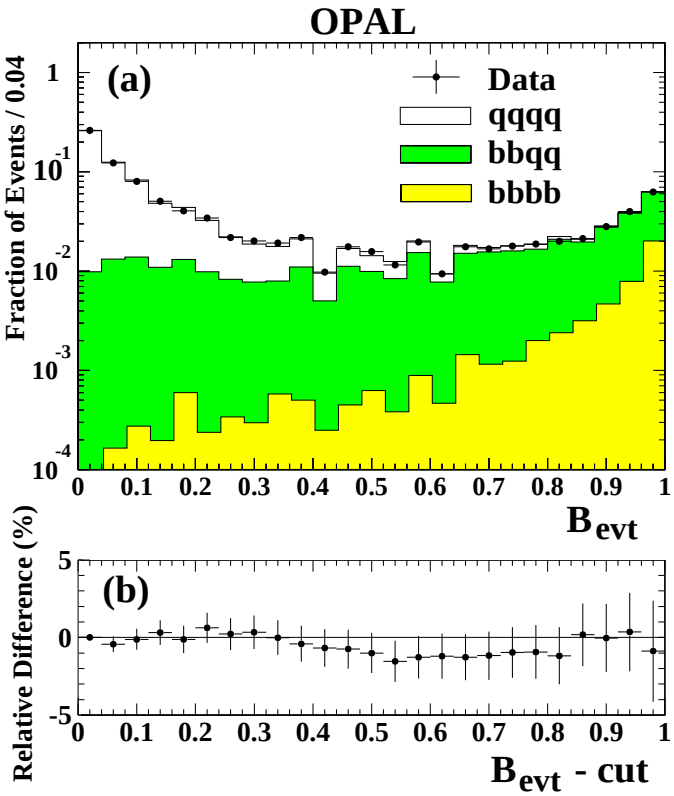

Fig. 4a,b. Four-jet channel: **a** the B_{evt} distribution for overlaid pairs of hadronic Z^0 decay events (described fully in the text). OPAL data are indicated by points (the error bars are smaller than the points), and the Monte Carlo simulation by the histograms with the contributions from final states containing four b-quarks (light), two b-quarks (dark) and only light flavoured quarks (open). The discontinuous behaviour in the central bins is due to the discrete binning of the two b-tag variables used as inputs to the likelihood. **b** The relative difference between OPAL data and the Monte Carlo simulation for the event b-tagging rate as a function of the cut on B_{evt} for pairs of overlaid Z^0 decays.

the following cross-check has been performed. The measured charged particle tracks and calorimeter clusters of pairs of hadronic Z^0 decay events recorded in 1998 at $\sqrt{s} = m_Z$ are overlaid to form pseudo-events which have topologies very similar to $e^+e^- \to Z^0Z^0 \to q\bar{q}q\bar{q}$ events at LEP2 energies. In order to model the b tag properly, the parameters of the tracks in the second Z^0 event are adjusted such that the reconstructed primary vertices of both overlaid events match. The same procedure is applied to simulated hadronic Z^0 decays. These pseudo-events are passed through the same analysis chain as the high energy data and Monte Carlo. The same preselection as described above is applied. The event b-tag likelihood B_{evt} is calculated using as inputs the two largest jet-wise b-tag variables – the same b-tag variables used in the h^0Z^0 selection. The distribution for B_{evt} is shown in Fig. 4 for overlaid data and overlaid Monte Carlo as well as their relative difference in the event tagging rate as a function of the cut on B_{evt}. The data and the Monte Carlo model agree to within 2%, independent of the cut on B_{evt}. Hence, no additional systematic error is assigned on the signal efficiency as a result of this cross-check.

4.2 The missing-energy channel

The preselection of the missing-energy analysis is designed to enhance a signal characterised by two hadronic jets and missing energy in the presence of radiative Z^0 events, untagged two-photon events and $W^+W^- \to q\bar{q}\ell\bar{\nu}_\ell$ events. These Standard Model backgrounds also can produce final states with two hadronic jets and missing energy, but they can be rejected because their missing momentum is predominantly along the beam axis (in the case of the radiative Z^0 events and untagged two-photon events), or there is a high-momentum lepton (in the case of $W^+W^- \to q\bar{q}\ell\bar{\nu}_\ell$ events). The preselection is described below.

The initial requirements are intended to suppress mismeasured events and two-photon and Z/γ^* backgrounds: (1) the number of tracks satisfying the quality requirements used in [14] must be greater than six and more than 20% of all tracks; there must be no significant energy in the forward detectors as described in [5]; there must be no hits in the MIP plug detector with a significant charge deposition; the total transverse momentum P^t_{vis} and the visible mass m_{vis} must satisfy $5 \cdot P^t_{\mathrm{vis}} + m_{\mathrm{vis}} > 100\,\mathrm{GeV}$; the total visible energy E_{vis} must not exceed 80% of $\sqrt{s}$; and there must be less than 50% of the visible energy in the angular region $|\cos\theta| > 0.90$. The following requirements reduce the Z/γ^* contribution: (2) the polar angle of the missing momentum, θ_{miss}, must satisfy $|\cos\theta_{\mathrm{miss}}| < 0.95$ and the z-component of the visible momentum must satisfy $|P^z_{\mathrm{vis}}| < 35\,\mathrm{GeV}$; (3) the tracks and clusters are grouped into two jets using the Durham algorithm, and the directions of both jets are required to satisfy $|\cos\theta_{\mathrm{jet}}| < 0.95$; (4) the acoplanarity angle[2] of the two jets, ϕ_{acop}, must be larger than 5°. The following requirements reduce the contribution from four-fermion processes: (5) the missing mass m_{miss} must be consistent with m_Z: $60\ \mathrm{GeV} < m_{\mathrm{miss}} < 120\,\mathrm{GeV}$; and (6) no identified isolated leptons, as defined in [5], may appear in the event.

The b-tag described in Sect. 3 is incorporated into the analysis by combining $\mathcal{B}_1$ and $\mathcal{B}_2$, the b-tagging discriminants of the two jets in the event, with four kinematic variables, $|\cos\theta_{\mathrm{miss}}|$, $\max(\cos\theta_{\mathrm{jet}})$, m_{miss}, and ϕ_{acop}, using the same likelihood technique as used at lower energies [4]. The high-p_t lepton tagging is removed from the calculation of the jet b-tagging discriminant variables $\mathcal{B}_i$ in order to avoid enhancing the $W^+W^- \to q\bar{q}\ell\bar{\nu}_\ell$ background in this search channel. Distributions of the kinematic and b-tag variables are shown in Fig. 5 for OPAL data and SM background simulations. The signal likelihood is required to be larger than 0.60 for an event to be selected as a Higgs boson candidate. In Fig. 6, the likelihood distribution and the mass distribution for the selected candidate events are shown for the data, SM backgrounds, and a simulated signal at $m_{\mathrm{h}} = 95\,\mathrm{GeV}$. The reconstructed Higgs boson mass

[2] The acoplanarity angle, ϕ_{acop}, of two vectors is 180° minus the opening angle between them in the plane transverse to the beam direction.

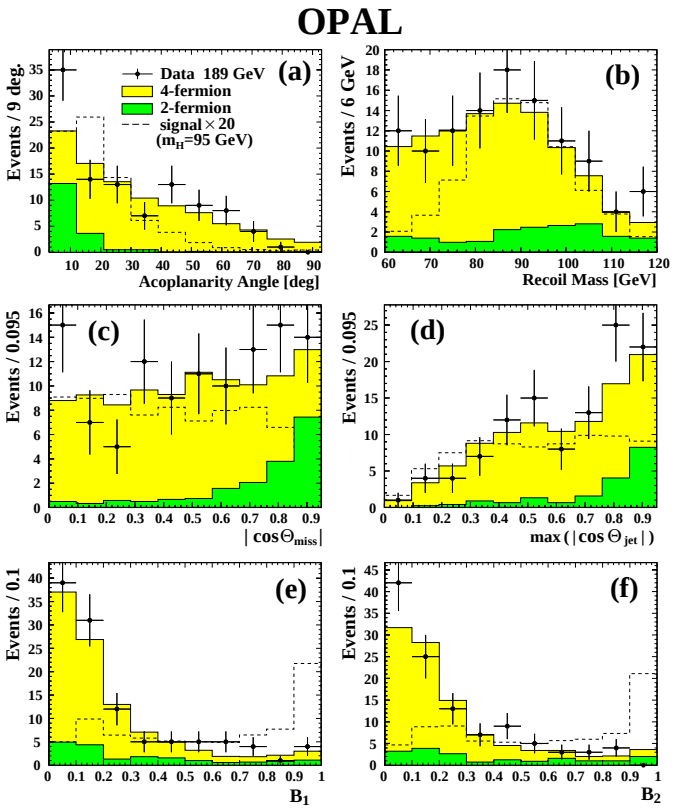

Fig. 5a–f. Input variables to the missing-energy channel likelihood selection: **a** the acoplanarity angle; **b** the invariant mass recoiling against the hadronic system; **c** the cosine of the polar angle of the missing momentum; **d** the larger cosine of the two jet polar angles; **e** and **f** the b-tags of the two jets. OPAL data are indicated by points with error bars, four-fermion backgrounds by the light grey histograms, and two-fermion backgrounds by the dark grey histograms. The estimated contribution from a 95 GeV higgs boson is shown with dashed histograms; it has been scaled up by a factor of 20.

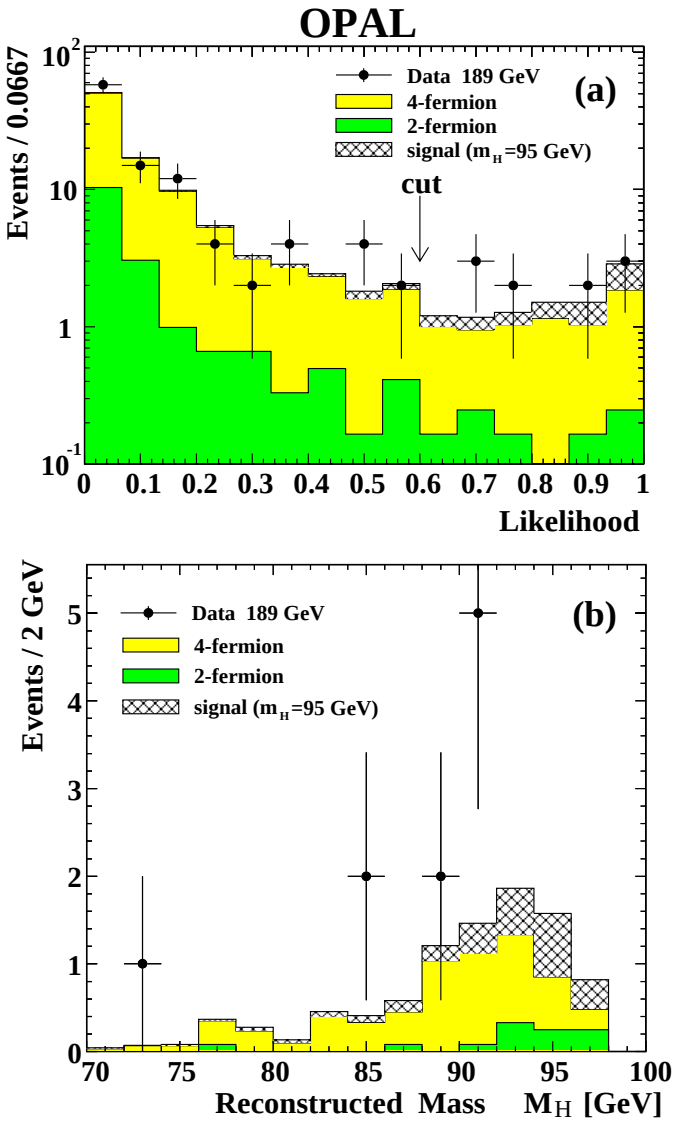

Fig. 6a,b. Missing-energy channel: **a** the likelihood distribution and **b** the reconstructed candidate masses. OPAL data are indicated by points with error bars, four-fermion backgrounds by the light grey histograms, and two-fermion backgrounds by the dark grey histograms. Also shown is the contribution expected from a 95 GeV Higgs boson (hatched histograms).

is evaluated using a kinematic fit constraining the recoil mass to the Z^0 mass.

The numbers of observed and expected events after each selection step are given[3] in Table 1. The selection efficiency estimated from the Monte Carlo for a 95 GeV Higgs particle is (35.4±0.9(stat.)±0.9(syst.))%. Ten events survive the selection and 6.9±0.5(stat.)±0.6(syst.) events are expected from SM background processes. The systematic error evaluation is described in [4]. The detection efficiency as a function of the Higgs boson mass is given in Table 4.

4.3 The tau channels

The tau channel selection consists of a preselection and tau lepton identification using an ANN, the details of which are described in [4]. The following preselection requirements are designed to separate the signal from Z/γ^* events. Each selected event must be a high-multiplicity multihadronic event [33], the direction of the missing momentum must satisfy $|\cos\theta_{\mathrm{miss}}| \leq 0.95$, the missing momentum p_{miss} must be less than $0.3 \cdot \sqrt{s}$, the scalar sum of the transverse momenta of the particles in the event must exceed 45 GeV, and at least one pair of oppositely-charged tau candidates must be identified.

The selection uses the two-tau likelihood of [4], $\mathcal{L}_{\tau\tau} = \frac{P_1 P_2}{P_1 P_2 + (1-P_1)(1-P_2)}$, where P_i is the probability that the i^{th} tau candidate originates from a real tau lepton. This probability is calculated from the shapes of the ANN output for signal and fake taus. The distribution of the ANN output

[3] In the calculation of the efficiencies and backgrounds in the missing-energy channel, a 2.5% relative reduction has been applied to the Monte Carlo estimates in order to account for accidental vetos due to accelerator-related backgrounds in the forward detectors.

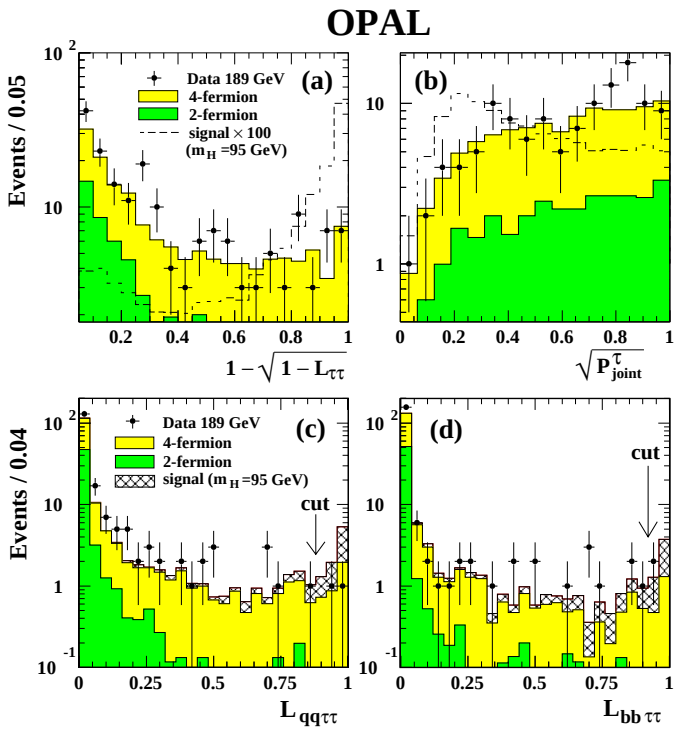

Fig. 7a–d. Tau channels: **a** distribution of the two-tau likelihood as input to the likelihood selection; **b** distribution of the joint impact parameter significance as input to the likelihood selection; **c** distribution of the $qq\tau\tau$ likelihood; **d** distribution of the $bb\tau\tau$ likelihood; OPAL data are indicated by points with error bars, four-fermion backgrounds by the light grey histograms, and two-fermion backgrounds by the dark grey histograms. Also shown is the contribution expected from a 95 GeV Higgs boson (dashed histograms in **a** and **b**, hatched histograms in **c** and **d**). In **a** and **b** the signal is scaled by a factor of 100.

for signal events was computed from Monte Carlo simulations. This analysis has been improved by using for the fake taus the distribution of the ANN output in hadronic Z^0 decay data collected at $\sqrt{s} \approx m_{Z^0}$, which has a low fraction of events with real taus. This estimation of the fake tau ANN distribution reduces the systematic uncertainty on the fake tau rate. To pass the selection, an event must have $\mathcal{L}_{\tau\tau}$ of at least 0.10.

Next, the particles in the events are subdivided into two tau candidates and two jets. A 2C kinematic fit is applied using total energy and momentum conservation constraints, where the tau momentum directions are taken from their visible decay products and their energies are unconstrained. The χ^2 probability of the fit is required to be larger than 10^{-5}. In events where both taus are classified as one-prong decays, the sum of the momenta of the charged particles assigned to the tau decays must be less than 80 GeV in order to reduce backgrounds from $Z^0Z^{0(*)} \to \mu^+\mu^- q\bar{q}$ and $Z^0Z^{0(*)} \to e^+e^- q\bar{q}$.

The two final likelihoods, described in [4], are then formed. One, $\mathcal{L}(b\bar{b}\tau^+\tau^-)$, is optimised for the $h^0Z^0 \to b\bar{b}\,\tau^+\tau^-$ final state and makes use of the b-tag of Sect. 3. The other, $\mathcal{L}(q\bar{q}\tau^+\tau^-)$, is optimised for the $h^0Z^0 \to \tau^+\tau^- q\bar{q}$ process and does not use b-tagging. The following variables described in [4] are inputs to both likelihoods: $R_{\rm vis} = E_{\rm vis}/\sqrt{s}$, $|\cos\theta_{\rm miss}|$, $\mathcal{L}_{\tau\tau}$, the logarithm of y_{34}, the energy of the most energetic electron or muon identified in the event (if any), the angles between each tau candidate and the nearest jet, and the logarithm of the larger of the two 3C kinematic fit probabilities, in which the additional constraint comes from fixing either the tau pair invariant mass or the jet pair invariant mass to the Z^0 mass. A new variable is introduced for this analysis which takes advantage of the finite lifetime of the tau lepton, the impact parameter information of the tracks belonging to the tau candidate, combined in a joint-probability calculation [34]. In addition to the above variables, the $\mathcal{L}(b\bar{b}\tau^+\tau^-)$ likelihood uses the output of the b-tagging algorithm described in Sect. 3. An event is retained if $\mathcal{L}(b\bar{b}\tau^+\tau^-)$ exceeds 0.92 or $\mathcal{L}(q\bar{q}\tau^+\tau^-)$ exceeds 0.88. Figure 7 shows the distributions of $\mathcal{L}_{\tau\tau}$, the joint impact-parameter probability, and the two likelihoods, $\mathcal{L}(q\bar{q}\tau^+\tau^-)$ and $\mathcal{L}(b\bar{b}\tau^+\tau^-)$, for the data, for the simulated Standard Model backgrounds, and also for a simulated 95 GeV Higgs signal.

The numbers of observed and expected events after each stage of the selection are given in Table 1, together with the detection efficiency for a 95 GeV SM Higgs boson, which is estimated to be $(34.3 \pm 1.1(\text{stat.}) \pm 2.4(\text{syst.}))\%$ after the final selection requirement. Three events survive the likelihood cut, to be compared to the expected background of $4.0 \pm 0.5(\text{stat.}) \pm 0.9(\text{syst.})$. The systematic errors are evaluated as in [4].

These results are confirmed by a separate analysis which uses a different technique to tag the tau candidates. Events are reconstructed as four jets using the Durham algorithm and tau candidates are sought in the four jets using a likelihood technique. The b-tagging algorithm of Sect. 3 is applied to the two remaining jets. This selection has a performance similar to that of the ANN method for tau tagging described above. The efficiency for a 95 GeV Higgs signal is evaluated to be $(30.6 \pm 1.1(\text{stat.}) \pm 1.6(\text{syst.}))\%$. Six events are retained, two of which are selected also by the analysis above, compared with the expected background of $3.0 \pm 0.5(\text{stat.}) \pm 0.6(\text{syst.})$ events.

4.4 The electron and muon channels

In approximately 6% of h^0Z^0 events the Z^0 is expected to decay into an electron pair or a muon pair. This topology is very distinct because the invariant mass of the lepton pair is expected to be close to the mass of the Z^0, and because of the presence of long-lived B hadrons in the two jets from the hadronic Higgs boson decay. The main source of irreducible background is expected to be from $Z^0Z^{0(*)}$ production, affecting the limits the most when the hypothesised Higgs boson mass is near the Z^0 boson mass. The selection is divided into two stages, a preselection and a likelihood selection.

The preselection for this analysis is intended to enhance the $\ell^+\ell^- q\bar{q}$ topology, where ℓ =e or μ. The requirements are listed below.

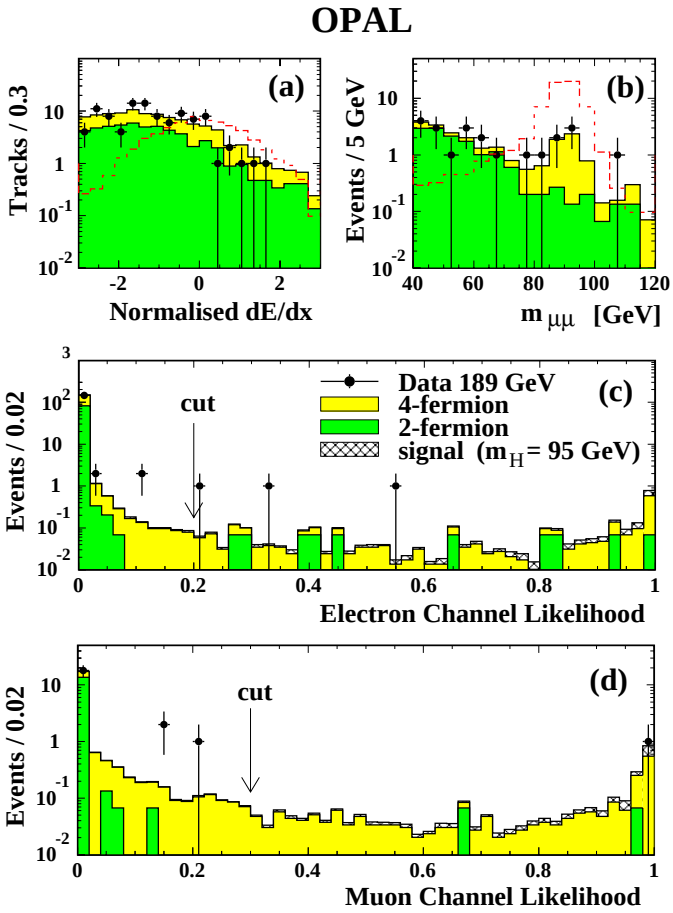

Fig. 8a–d. Electron and Muon channels: **a** The distribution of the normalised $\mathrm{d}E/\mathrm{d}x$, the difference between the ionisation energy loss of a track and that expected for an electron, divided by the measurement error, for tracks in the high-energy data. **b** Reconstructed invariant mass of identified muon pairs, where the signal is expected to contribute near $m_{\mu\mu} = m_{\mathrm{Z}^0}$. **c** The electron channel likelihood distribution, and **d** the muon channel likelihood distribution. OPAL data are indicated by points with error bars, four-fermion backgrounds by the light grey histograms, and two-fermion backgrounds by the darker grey histograms. The contribution from a 95 GeV Higgs boson signal is shown with dashed histograms in **a** and **b** and with hatched histograms in **c** and **d**. It is scaled by a factor of 100 in **a** and **b**.

1. The event must have at least six charged particle tracks, $y_{34} > 10^{-4}$, $|P^z_{\mathrm{vis}}| < (E_{\mathrm{vis}} - 0.5\sqrt{s})$ and $E_{\mathrm{vis}} > 0.6\sqrt{s}$.
2. At least one pair of oppositely charged leptons of the same flavour (e or μ) must be identified as described in [5]. If more than one such pair is found, the pair for which the invariant mass is closest to the mass of the Z^0 is used in the subsequent steps of the selection. Figure 8a shows the distribution of the normalised $\mathrm{d}E/\mathrm{d}x$, an important ingredient of the electron identification.
3. The tracks and clusters not associated with the selected lepton pair are grouped into two jets using the Durham algorithm. In the case of the muon channel, a 4C kinematic fit, requiring total energy and momentum conservation, is applied to improve the mass resolution of the muon pair and is required to yield a χ^2 probability larger than 10^{-5}. The invariant mass of the lepton pair is required to be larger than 40 GeV. The distribution of reconstructed dimuon masses is shown in Fig. 8b.

Table 2. Signal detection efficiencies for the searches for the SM Higgs boson, applied to the processes with $\mathrm{h}^0 \to \mathrm{A}^0\mathrm{A}^0$ followed by $\mathrm{A}^0 \to \mathrm{b\bar{b}}$. The efficiencies are quoted for $m_{\mathrm{h}} = 70\,\mathrm{GeV}$ and $m_{\mathrm{A}} = 20\,\mathrm{GeV}$. The statistical errors due to the limited sizes of the Monte Carlo samples are 1–4%. The backgrounds and candidates for each channel are listed in Table 1.

SM search	applied to the process	Efficiency (%)
four jet	$(\mathrm{A}^0\mathrm{A}^0 \to \mathrm{b\bar{b}b\bar{b}})(\mathrm{Z}^0 \to \mathrm{q\bar{q}})$	20
missing energy	$(\mathrm{A}^0\mathrm{A}^0 \to \mathrm{b\bar{b}b\bar{b}})(\mathrm{Z}^0 \to \nu\bar{\nu})$	32
tau lepton	$(\mathrm{A}^0\mathrm{A}^0 \to \mathrm{b\bar{b}b\bar{b}})(\mathrm{Z}^0 \to \tau^+\tau^-)$	38
electron	$(\mathrm{A}^0\mathrm{A}^0 \to \mathrm{b\bar{b}b\bar{b}})(\mathrm{Z}^0 \to \mathrm{e}^+\mathrm{e}^-)$	60
muon	$(\mathrm{A}^0\mathrm{A}^0 \to \mathrm{b\bar{b}b\bar{b}})(\mathrm{Z}^0 \to \mu^+\mu^-)$	73

Two likelihoods, one based on kinematic variables, $\mathcal{K}$, and one for b-tagging for the two jets of hadrons, $\mathcal{B}_{2\mathrm{jet}}$, are calculated as described in [4]. The final signal likelihood is computed using $\mathcal{K}$ and $\mathcal{B}_{2\mathrm{jet}}$ as inputs. The combined likelihood is required to exceed 0.2 for the electron channel and 0.3 for the muon channel. Distributions of these likelihoods are shown in Fig. 8. The signal selection efficiency for a 95 GeV SM Higgs boson is $(55.0 \pm 0.9(\mathrm{stat.}) \pm 1.1(\mathrm{syst.}))\%$ for the electron channel, and $(64.9 \pm 0.9(\mathrm{stat.}) \pm 0.9(\mathrm{syst.}))\%$ for the muon channel. The numbers of observed and expected events after each stage of the selection are given in Table 1, together with the detection efficiencies for a 95 GeV SM Higgs boson. The selection retains three events in the electron channel and one in the muon channel. The total background expectation is $2.6 \pm 0.2(\mathrm{stat.}) \pm 0.5(\mathrm{syst.})$ events in the electron channel and $2.1 \pm 0.1(\mathrm{stat.}) \pm 0.4(\mathrm{syst.})$ events in the muon channel.

4.5 Search for the MSSM process $\mathrm{h}^0\mathrm{Z}^0$ with $\mathrm{h}^0 \to \mathrm{A}^0\mathrm{A}^0$

If $2m_{\mathrm{A}} \leq m_{\mathrm{h}}$, the decay $\mathrm{h}^0 \to \mathrm{A}^0\mathrm{A}^0$ is kinematically allowed and is the dominant decay of the h^0 in parts of MSSM parameter space. Dedicated, optimised searches for $\mathrm{h}^0\mathrm{Z}^0 \to \mathrm{A}^0\mathrm{A}^0\mathrm{Z}^0$ have not been performed. Instead, the sensitivities of the $\mathrm{h}^0\mathrm{Z}^0$ searches to processes with $\mathrm{h}^0 \to \mathrm{A}^0\mathrm{A}^0$ have been evaluated by studying the efficiencies of the selections using a $\mathrm{h}^0\mathrm{Z}^0 \to \mathrm{A}^0\mathrm{A}^0\mathrm{Z}^0 \to \mathrm{b\bar{b}b\bar{b}Z}^0$ Monte Carlo. Non-$\mathrm{b\bar{b}}$ decays of the A^0 are not considered. The efficiencies of the $\mathrm{h}^0\mathrm{Z}^0$ selections for the process $\mathrm{h}^0\mathrm{Z}^0 \to \mathrm{A}^0\mathrm{A}^0\mathrm{Z}^0$ with $m_{\mathrm{A}} = 20\,\mathrm{GeV}$ and $m_{\mathrm{h}} = 70\,\mathrm{GeV}$ are summarised in Table 2. In general, the efficiency is found to increase with the h^0 mass. This procedure has the advantage of simplifying the statistical treatment and is sufficiently powerful to exclude regions in which the decay $\mathrm{h}^0 \to \mathrm{A}^0\mathrm{A}^0 \to \mathrm{b\bar{b}b\bar{b}}$ dominates. The expected backgrounds and the selected candidates are the same as for the results described above, since the same selections are applied.

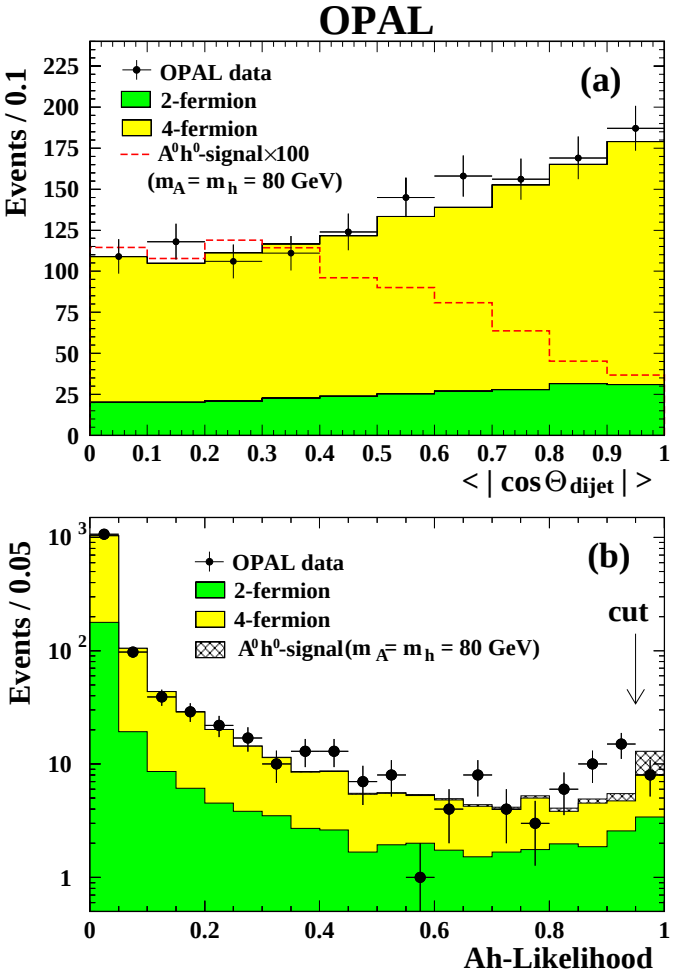

Fig. 9. **a** The distribution of $\langle|\cos\Theta_{\mathrm{dijet}}|\rangle$ for the $\mathrm{A^0h^0}\to\mathrm{b\bar{b}b\bar{b}}$ channel. **b** The distribution of the selection likelihood in the $\mathrm{A^0h^0}\to\mathrm{b\bar{b}b\bar{b}}$ channel. OPAL data are indicated by points with error bars, four-fermion backgrounds by the light grey histograms, and two-fermion backgrounds by the dark grey histograms. Also shown is the contribution expected from a Higgs boson signal with $m_{\mathrm{h}} = m_{\mathrm{A}} = 80\,\mathrm{GeV}$ (other MSSM parameters are set to their "benchmark" values with maximal scalar top mixing, as described in Sect. 6.2) as dashed **a** and hatched **b** histograms. In **a** the signal is scaled by a factor of 100.

5 The $\mathrm{A^0h^0}$ search channels

Searches are presented for the MSSM process of associated production $\mathrm{e^+e^-}\to\mathrm{A^0h^0}$ followed by the decays $\mathrm{A^0h^0}\to\mathrm{b\bar{b}\,b\bar{b}}$ and $\mathrm{A^0h^0}\to\mathrm{b\bar{b}}\tau^+\tau^-$. If $\mathrm{h^0}\to\mathrm{A^0A^0}$ is kinematically allowed, the process $\mathrm{e^+e^-}\to\mathrm{A^0h^0}\to\mathrm{A^0A^0A^0}$ is also sought in the $\mathrm{b\bar{b}b\bar{b}b\bar{b}}$ final state. These selections differ from those for $\mathrm{Z^0h^0}$ because the $\mathrm{Z^0}$ mass constraint is no longer applicable. The selections therefore have been optimised to reject backgrounds differing kinematically from those important to the $\mathrm{Z^0h^0}$ searches.

5.1 The $\mathrm{A^0h^0}\to\mathrm{b\bar{b}b\bar{b}}$ final state

The same preselection requirements are applied as described in [4]. These are:

1–3. The requirements 1–3 of the $\mathrm{h^0Z^0}$ four-jet analysis of Sect. 4.1 are used.
4. The C-parameter must be larger than 0.45.
5. Each of the four jets must contain at least six energy-flow objects and at least one track.
6. The χ^2 probability of a 4C fit, which requires energy and momentum conservation, must be larger than 10^{-5}.

For events passing the preselection, a likelihood technique is applied as described in [4]. Seven input variables are used. Six of these variables are the same as those used in [4]: the four b-tagging discriminants $\mathcal{B}_i$, one for each jet (see Sect. 3), y_{34} in the Durham scheme and the event thrust. The seventh variable is $\langle|\cos\Theta_{\mathrm{dijet}}|\rangle$, the average absolute value of the cosines of the polar angles of the momenta of the two di-jet systems for the combination yielding the smallest difference in the two di-jet invariant masses after the 4C kinematic fit. This last variable replaces the mean $|\cos\theta_{\mathrm{jet}}|$ of the four jets used in [4] because it provides better discrimination against the $\mathrm{W^+W^-}$ background. The distribution of $\langle|\cos\Theta_{\mathrm{dijet}}|\rangle$ is shown in Fig. 9, along with the final likelihood discriminant $\mathcal{L}^{\mathrm{Ah}}$.

Candidate events are selected by requiring $\mathcal{L}^{\mathrm{Ah}} > 0.95$. Table 3 shows the numbers of selected events together with the expectation from background processes and the signal selection efficiency for $m_{\mathrm{A}} = m_{\mathrm{h}} = 80\,\mathrm{GeV}$, after each cut in the preselection and after the final cut on $\mathcal{L}^{\mathrm{Ah}}$. The detection efficiency for an $\mathrm{A^0h^0}$ signal with masses $m_{\mathrm{A}} = m_{\mathrm{h}} = 80\,\mathrm{GeV}$ is estimated to be $(48.4\pm0.7(\mathrm{stat.})\pm3.9(\mathrm{syst.}))\%$. Eight candidate events are observed in the data, consistent with $8.0\pm0.5(\mathrm{stat.})\pm1.4(\mathrm{syst.})$ events expected from SM background processes. Six of the candidate events are common to those found in the SM four-jet channel of Sect. 4.1. The systematic uncertainties on the signal selection efficiencies and background estimates were determined using the same methods as described in [4].

Candidate Higgs boson masses are calculated from the measured jet momenta using the 4C fit. Figure 10a–c shows the distribution of the sum of the reconstructed Higgs boson masses, $M_{\mathrm{sum}} \equiv m_{\mathrm{h}}^{\mathrm{rec}} + m_{\mathrm{A}}^{\mathrm{rec}}$, for all three possible di-jet pairings, separately according to the reconstructed mass difference, $\Delta M \equiv |m_{\mathrm{A}}^{\mathrm{rec}} - m_{\mathrm{h}}^{\mathrm{rec}}|$. The resolution on the mass sum, M_{sum}, is estimated to be approximately 3 GeV for $m_{\mathrm{h}} + m_{\mathrm{A}} = 150$ GeV. For $m_{\mathrm{h}} = m_{\mathrm{A}}$, 68% of the events have a reconstructed mass difference ΔM of less than 13 GeV. Since the four jets can be combined in three ways, and since the $\mathrm{h^0}$ and $\mathrm{A^0}$ cannot be distinguished, each candidate event enters at six points in the $(m_{\mathrm{h}},m_{\mathrm{A}})$ plane.

5.2 The $\mathrm{A^0h^0}\to\mathrm{b\bar{b}}\tau^+\tau^-$ final state

The $\mathrm{A^0h^0}\to\mathrm{b\bar{b}}\tau^+\tau^-$ final state, where either the $\mathrm{A^0}$ or the $\mathrm{h^0}$ decays into a tau pair, has been searched for using the

Table 3. The A^0h^0 channels: effect of the cuts on data and the simulated background, normalised to the integrated luminosity of the data. The two-photon backgrounds, not shown separately, are included in the total background. The signal efficiencies are given in the last column for m_h=m_A=80 GeV in the $A^0h^0 \to b\bar{b}b\bar{b}$ and the tau channels and for $m_h = 70\,\mathrm{GeV}$ and $m_A = 20\,\mathrm{GeV}$ in the $A^0h^0 \to A^0A^0A^0 \to b\bar{b}b\bar{b}b\bar{b}$ channel

.

Cut	Data	Total bkg.	$q\bar{q}(\gamma)$	4-fermi.	Efficiency (%)
$A^0h^0 \to b\bar{b}b\bar{b}$	Channel	172.1 pb^{-1}			$m_A = m_h = 80$ GeV
(1)	18701	18120	14716	3200	99.9
(2)	6242	6183	4215	1954	95.6
(3)	1955	1891	538	1353	91.2
(4)	1668	1606	316	1290	83.3
(5)	1464	1402	273	1128	83.3
(6)	1382	1335	251	1084	81.3
$\mathcal{L}^{Ah} > 0.95$	8	8.0	3.4	4.6	48.4
$A^0h^0 \to b\bar{b}\tau^+\tau^-$	168.7 pb^{-1}				$m_A = m_h = 80$ GeV
Pre-sel	4652	4584	2809	1767	83.8
$\mathcal{L}_{\tau\tau}$	733	693	100	590	69.4
2C fit	201	160	56	104	55.2
1-prong E sum	185	156	55	101	54.8
Final $\mathcal{L}$	7	4.9	0.4	4.5	45.3
$A^0h^0 \to A^0A^0A^0 \to b\bar{b}b\bar{b}b\bar{b}$	Channel	172.1 pb^{-1}			(m_h, m_A)=(70,20) GeV
Pre-sel	1841	1740	1205	535	90.4
Kin-ANN	649	591	438	153	82.6
btag-ANN	5	8.7	7.7	1.0	45.4

same technique as used in the SM tau channels described above. The final likelihood selection has been optimised for the MSSM process.

The following variables are used as inputs to the calculation of the likelihood, $\mathcal{L}_{hA}$: R_{vis}, $|\cos\theta_{miss}|$, $\mathcal{L}_{\tau\tau}$, the logarithm of y_{34}, the energy of the most energetic identified electron or muon, the tau-track lifetime information as described in Sect. 4.3, the average of the absolute values of the cosines of the polar angles of the reconstructed h^0 and A^0, which gives an estimate of the production angle of the two Higgs bosons, and the outputs of the b-tagging algorithm described in Sect. 3 for the two hadronic jets in the event.

Candidate events are selected by requiring the final likelihood value to exceed 0.64. Table 3 shows the number of selected events, the efficiency for $m_h = m_A = 80\,\mathrm{GeV}$ and the background estimation, after each stage of the selection. The efficiency for a signal with $m_h = m_A = 80\,\mathrm{GeV}$ is estimated to be $(45.3\pm1.5(\mathrm{stat.})\pm2.3(\mathrm{syst.}))\%$. Seven candidates are observed in the data, two of which are shared with the SM analysis of Sect. 4.3. The number of events expected from SM background processes is $4.9 \pm 0.6(\mathrm{stat.})\pm1.6(\mathrm{syst.})$. The distribution of the sum of the reconstructed Higgs boson masses, $M_h^{rec} + M_A^{rec}$, is shown in Fig. 10d. Since the A^0 and h^0 cannot be distinguished, each selected event has two interpretations in the (m_h, m_A) plane. Systematic uncertainties on backgrounds and efficiencies are evaluated as in Sect. 4.3.

The alternative jet-based analysis, described in Sect. 4.3, is also applied in this search channel. This procedure gives an overall efficiency of $(39.1\pm1.5)\%$ for $m_h = m_A = 80\,\mathrm{GeV}$, similar to that obtained above with the ANN tau identification, and the efficiency remains similar over the range of kinematically allowed values of m_h and m_A. The choice of the ANN analysis has been made to optimise the expected limits. Five events, two of which are shared with the ANN analysis, meet the selection requirements of the alternative analysis, consistent with the expectation of $4.8 \pm 0.6(\mathrm{stat.})\pm0.9(\mathrm{syst.})$ from SM background processes.

5.3 The $A^0h^0 \to A^0A^0A^0 \to b\bar{b}b\bar{b}b\bar{b}$ final state

Signal events in this decay mode are characterised by a large number of jets containing b-flavoured hadrons. Backgrounds are reduced through cuts on kinematic variables and by b-tagging. Signal events satisfy $2m_A \leq m_h$, and this analysis uses an ANN to optimise the sensitivity over the allowed mass region in the (m_h,m_A) plane.

The analysis begins with a set of preselection requirements. Events must be selected as hadronic final states [33]. The polar angle of the thrust axis, θ_T, must satisfy $|\cos\theta_T| \leq 0.9$. The charged particle tracks and clusters are grouped into six jets using the Durham [15] algorithm. Each jet is required to have at least one track and one electromagnetic cluster. Events must have at least 20 good

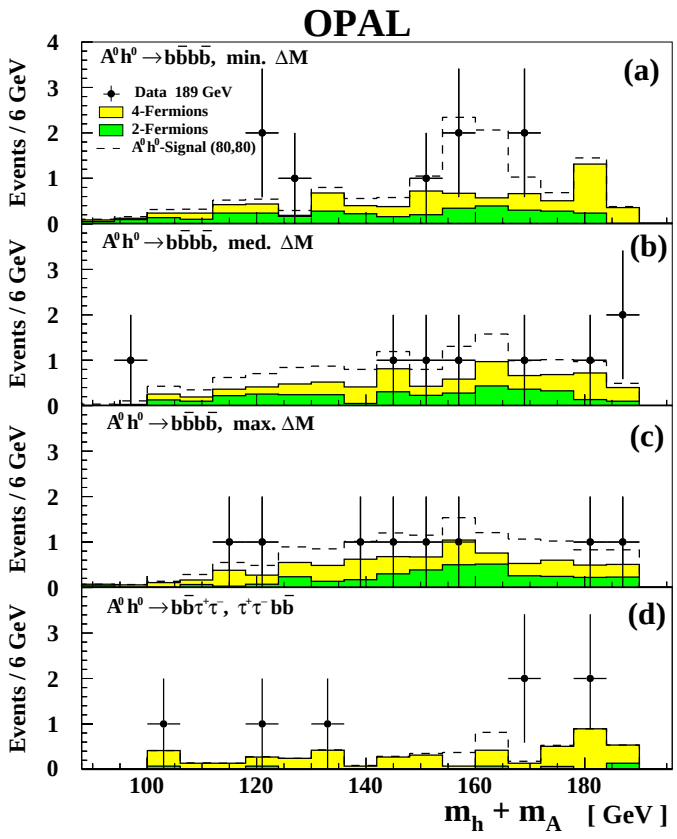

Fig. 10a–d. The sum of the reconstructed Higgs boson masses, $m_A^{rec} + m_h^{rec}$, for **a** the $A^0h^0 \to b\bar{b}b\bar{b}$ channel with the di-jet pairing combination which yields the smallest mass difference, $\Delta M \equiv |m_A^{rec} - m_h^{rec}|$, **b** the $A^0h^0 \to b\bar{b}b\bar{b}$ channel with the medium ΔM combination, **c** the $A^0h^0 \to b\bar{b}b\bar{b}$ channel with the maximum ΔM combination, and **d** the $A^0h^0 \to \tau^+\tau^- b\bar{b}, b\bar{b}\tau^+\tau^-$ channel. OPAL data are indicated by points with error bars, four-fermion backgrounds by the light grey histograms, and two-fermion backgrounds by the darker grey histograms. Also shown as dashed histograms are the contributions expected from a Higgs boson signal with $m_h = m_A = 80\,\mathrm{GeV}$ (other MSSM parameters are set to their "benchmark" values with maximal scalar top mixing, as described in Sect. 6.2).

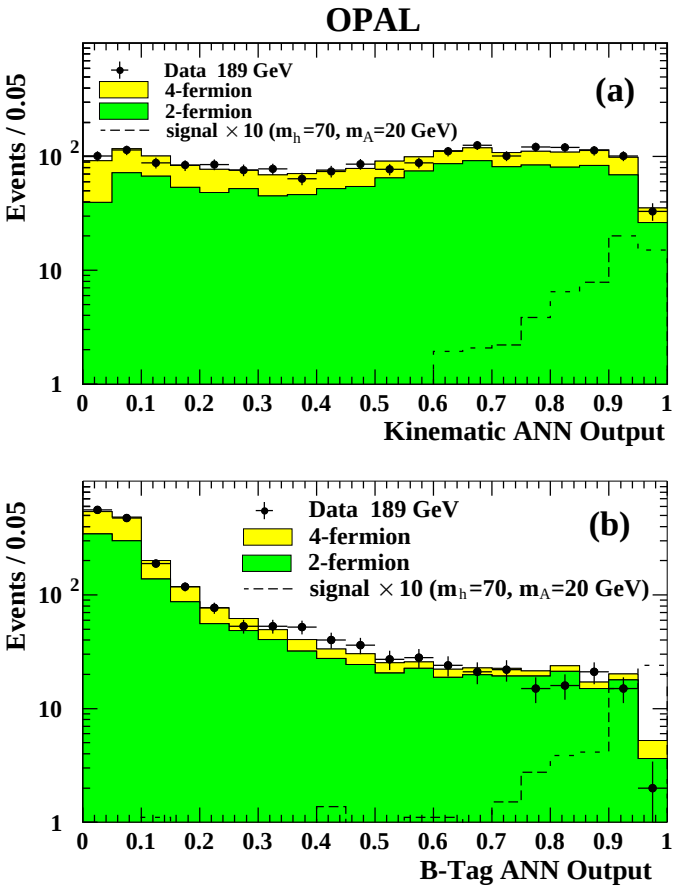

Fig. 11a,b. $e^+e^- \to A^0h^0 \to A^0A^0A^0 \to b\bar{b}b\bar{b}b\bar{b}$ channel: The distribution of the ANNs with kinematic variables **a** and with b-tagging variables **b**, as described in the text. The light grey histograms indicate Standard Model $q\bar{q}$ background, and the dark grey histograms show the distributions of Standard Model four-fermion background. The dashed histograms show the distribution from a signal Monte Carlo with Higgs boson masses of m_h=70 GeV and m_A=20 GeV (other MSSM parameters are set to their "benchmark" values with maximal scalar top mixing, as described in Sect. 6.2) scaled by a factor of 10.

quality tracks and at least 20 good quality electromagnetic calorimeter clusters, where the quality requirements are those used in [14]. To suppress the background from $(Z/\gamma)^*$, the value of y_{34} is required to be larger than 0.0005 and the C-parameter is required to be larger than 0.0075.

After the preselection, candidates are selected using two neural networks applied sequentially, one combining kinematic and topological variables, and one for the b-tagging variables. The kinematic characteristics of signal events depend strongly on m_h and m_A, and in order to maintain good sensitivity over a broad range of these masses, 14 variables with complementary discriminating roles are used as inputs for the first network. These are the event thrust, sphericity, oblateness, C and D parameters [30], the 2nd through the 6th normalised Fox-Wolfram [35] moments, and y_{23}, y_{34}, y_{45} and y_{56} for the Durham scheme. Events were required to have a kinematic network output greater than 0.68.

The final selection was made with an ANN optimised for b-tagging. If the A^0 is light, the two jets originating from the A^0 decay may be observed as a single jet; events then may seem to have only three jets. The events are therefore reconstructed both as three and six jets and a 15-input neural network has been trained using the b-tag variables described in Sect. 3, from the three and six jets in the event. Events are required to have a b-tagging network output greater than 0.92. The distributions of the two network outputs are shown in Fig. 11 for events passing the preselection.

Five events pass all selection requirements (Table 3), consistent with an expected background of 8.7 ± 1.0(stat.) $\pm$ 2.5(syst.) events. The signal efficiency for m_A=20 and m_h=70 GeV is (45.4±2.2(stat.)±4.3(syst.))%. The systematic errors are evaluated similarly to those for the

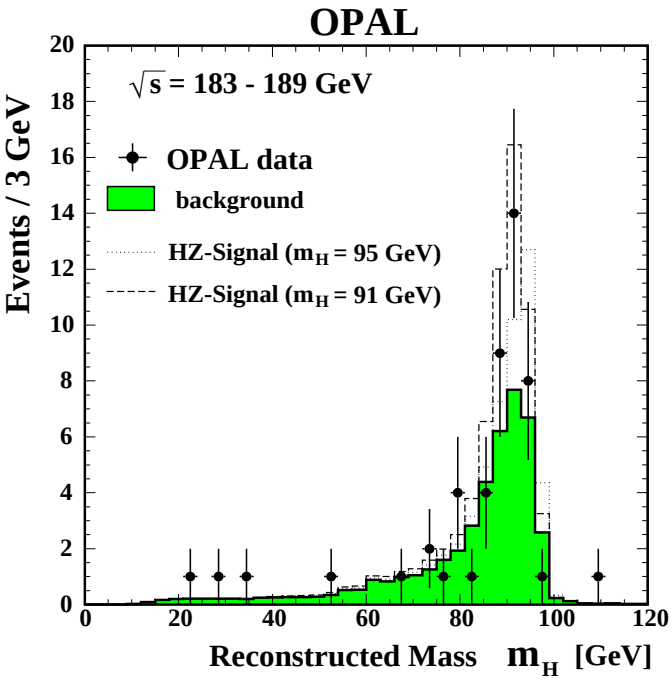

Fig. 12. The mass distribution for the selected events in all h^0Z^0 channels combined (points with error bars), and the expected background. The data and expected backgrounds have been combined for the $\sqrt{s} = 183\,\mathrm{GeV}$ and $\sqrt{s} = 189\,\mathrm{GeV}$ samples. The expected mass distribution assuming the production of the SM Higgs boson with a mass of 91 GeV (95 GeV) is added on top of the background and shown with a dashed (dotted) histogram.

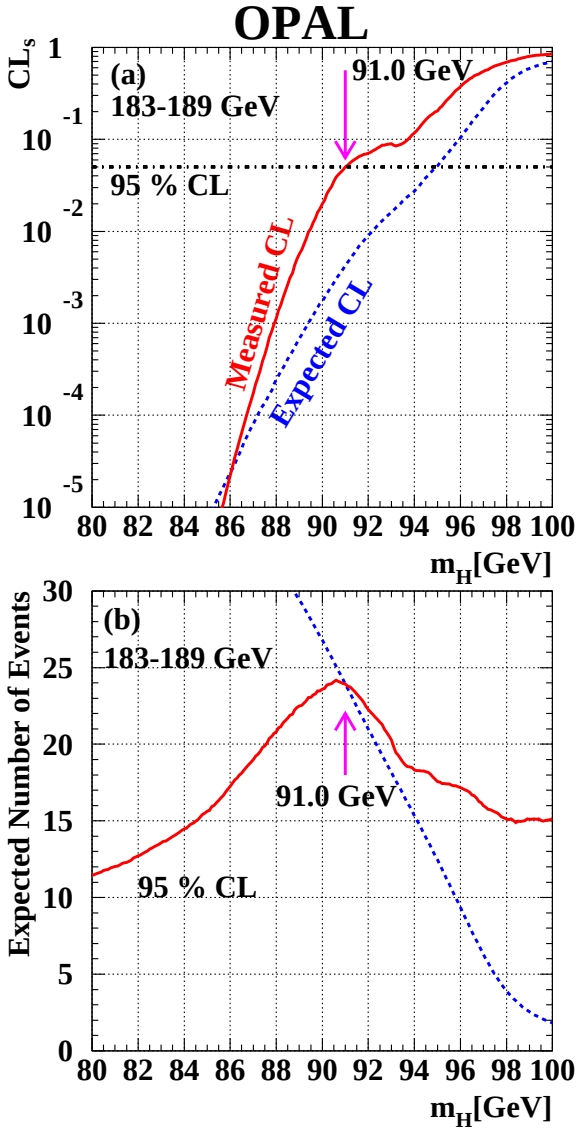

Fig. 13a,b. Limits on the mass of the Standard Model Higgs boson H^0_{SM}: **a** The confidence level for the signal hypothesis as observed (solid line) and expected on average for background-only experiments (dashed line), as functions of the SM Higgs boson mass. **b** The limit on the production rate for the SM Higgs boson at 95% CL (solid line) and the number of expected signal events (dashed line) as functions of the Higgs boson mass. The 95% CL lower mass limit on the SM Higgs bosons is set at the point where the solid and dashed curve intersect: $m_H > 91.0\,\mathrm{GeV}$.

other channels [4]. The dominant contribution to the systematic error on the signal and background efficiencies comes from the uncertainty related to the b-tagging. The main components arise from uncertainties in the tracking performance of the detector and the b-hadron decay multiplicity [36].

6 Limits

6.1 Mass limit for the SM Higgs boson

The efficiencies and numbers of expected SM Higgs signal and background events are summarised in Table 4, separately for 189 GeV and with the 183 GeV sample [4] added. In the 189 GeV data sample, 41 events pass the selections and $35.4 \pm 1.1(\mathrm{stat.}) \pm 3.2(\mathrm{syst.})$ events are expected from the SM background processes. The reconstructed masses of the candidate events and the distribution expected for the combined SM backgrounds for the searches presented here, added to those from our $\sqrt{s} \approx 183\,\mathrm{GeV}$ searches [4], are shown in Fig. 12. A slight excess of events peaks at the Z^0 mass, which is consistent with a statistical fluctuation of the dominant Z^0Z^0 background.

To derive a lower bound on the mass of the SM Higgs boson, the results of the searches presented here are combined with those of OPAL's earlier searches at $\sqrt{s} \approx 183\,\mathrm{GeV}$ [4]. Searches at energies of 172 GeV and lower have a negligible impact on the expected limit because the expected cross-sections for SM Higgs boson production are very small in those samples for Higgs boson masses near the limit expected from the searches at 183 and 189 GeV, and because the integrated luminosities collected at $\sqrt{s} \approx 172\,\mathrm{GeV}$ and $\sqrt{s} \approx 161\,\mathrm{GeV}$ are smaller. The systematic errors on the background expectations and on the signal selection efficiencies have been treated following the method given in [37]. The confidence level for the sig-

Table 4. Detection efficiencies in percent and numbers of expected SM Higgs boson events (in parentheses), at $\sqrt{s} = 189\,\mathrm{GeV}$, for each search channel separately, as a function of the Higgs boson mass. The last two rows show the sum of expected SM backgrounds, the error on the background sum, and the numbers of candidates, for each channel separately. The last two columns show the total numbers of expected events in all channels for the present search at $\sqrt{s} = 189\,\mathrm{GeV}$, and also summed with the results obtained at 183 GeV [4].

m_{H}	$\mathrm{q\bar{q}H^0_{SM}}$	$\nu\bar{\nu}\mathrm{H^0_{SM}}$	$\tau^+\tau^-\mathrm{q\bar{q}}$	$\mathrm{e^+e^-H^0_{SM}}$	$\mu^+\mu^-\mathrm{H^0_{SM}}$	Expected signal	
GeV	$\mathrm{H^0_{SM}}\to\mathrm{b\bar{b}}$					189 GeV	total
70	18.0 (14.96)	29.8 (8.75)	29.9 (3.56)	54.8 (2.65)	61.3 (2.81)	32.73	48.23
75	21.3 (15.38)	33.3 (8.52)	31.1 (3.24)	50.2 (2.11)	58.6 (2.35)	31.61	45.45
80	30.4 (18.28)	36.7 (7.87)	32.2 (2.83)	52.2 (1.84)	59.5 (1.99)	32.82	44.02
85	37.7 (17.91)	39.1 (6.67)	33.1 (2.31)	54.7 (1.53)	62.1 (1.65)	30.08	37.93
90	44.4 (14.86)	39.0 (4.78)	34.1 (1.69)	56.1 (1.12)	64.5 (1.22)	23.67	27.08
95	47.0 (7.76)	35.4 (2.25)	34.3 (0.85)	55.0 (0.56)	64.9 (0.61)	12.03	12.56
100	39.0 (0.99)	27.0 (0.38)	29.0 (0.11)	38.0 (0.08)	61.4 (0.09)	1.65	1.85
Bkg.	19.9	6.9	4.0	2.6	2.1	35.4	43.9
σ_{sys}	±3.0	±0.8	±1.0	±0.5	±0.4	±3.3	±3.4
Data	24	10	3	3	1	41	50

nal hypothesis, CL_s, is shown in Fig. 13a. It has been computed using the weighted event-counting method described in Sect. 5 of [6].

The number of expected signal events and the upper limit on the production rate for signal events at the 95% confidence level (CL) are given in Fig. 13b as functions of the Higgs boson mass hypothesis. A lower mass bound of 91.0 GeV is obtained at the 95% CL, while the average expected limit from a large number of fictitious experiments assuming the background-only (zero signal) hypothesis is 94.9 GeV. The probability to obtain a limit of 91.0 GeV or less in an ensemble of background-only experiments is 4%.

6.2 Limits in the MSSM parameter space

The searches presented in this publication at $\sqrt{s} \approx 189$ GeV are combined with previous OPAL Higgs boson searches [4–6,38–40] using data taken with $\sqrt{s} \leq 184\,\mathrm{GeV}$. We present 95% CL limits in the MSSM parameter space for the constrained MSSM with six parameters, m_0, M_2, A, μ, $\tan\beta = v_2/v_1$ and m_{A} in addition to those of the SM. The definitions of these parameters can be found in [6]. The consistency of the predictions of the constrained MSSM with our observed data has been calculated for a large sample of models in the space spanned by these six parameters. The scanning strategy is described in detail in [6].

A subset of the model space used for setting "benchmark" limits (Scan A of [6]) is defined by considering $\tan\beta$ between 0.7 to 50.0 and m_{A} between 5.0 GeV and 2000.0 GeV, while choosing fixed values for the remaining parameters. The soft SUSY breaking mass parameters at the electroweak scale (*e.g.*, m_{Q}, the "left-up" scalar quark mass) are set to 1.0 TeV and M_2 is set[4] to 1.63 TeV. These values were chosen in order to decouple the limits for Higgs boson production from the phenomenology of supersymmetric partners of Standard Model fermions and gauge bosons. The parameter μ is fixed to $-100\,\mathrm{GeV}$, and the mass of the top quark is assumed to be 175 GeV. Two cases of scalar top quark mixing are considered, one in which A is set to 0 GeV, corresponding to no mixing, and the other in which $A = \sqrt{6}m_{\mathrm{Q}}$, corresponding to maximal mixing. The excluded subsets of the benchmark model space are shown in Fig. 14 in the (m_{h},m_{A}) plane, the (m_{h},$\tan\beta$) plane[5], and the (m_{A},$\tan\beta$) plane. Both cases of scalar top mixing are included. If for either choice of the mixing a parameter set is not excluded, the point is shown as unexcluded.

For $\tan\beta > 1$, lower mass limits of $m_{\mathrm{h}} > 74.8\,\mathrm{GeV}$ and $m_{\mathrm{A}} > 76.5\,\mathrm{GeV}$ are obtained, while the expected limits are $m_{\mathrm{h}} > 76.4\,\mathrm{GeV}$ and $m_{\mathrm{A}} > 78.2\,\mathrm{GeV}$. In the case of no scalar top mixing, we exclude the range $0.72 < \tan\beta < 2.19$, while no $\tan\beta$ is excluded in the case of maximal scalar top mixing. For smaller m_{top} the excluded region of $\tan\beta$ becomes larger, while for larger m_{top}, it becomes smaller. If $\tan\beta$ is allowed to vary between 0.7 and 1.0, the range of possibilities in the model is larger and a small, unexcluded region appears at $m_{\mathrm{h}} \approx 70\,\mathrm{GeV}$, $m_{\mathrm{A}} < 10\,\mathrm{GeV}$ and $\tan\beta \approx 0.7$. In this region the model predicts the dominant decay mode of the $\mathrm{h^0}$ to be $\mathrm{h^0}\to\mathrm{A^0A^0}$. For the same model points, the $\mathrm{A^0}$ is not massive enough to decay into $\mathrm{b\bar{b}}$, rendering the analyses of this paper inefficient. Nearby regions are excluded because the decay $\mathrm{h^0}\to\mathrm{b\bar{b}}$ proceeds, although with a reduced branching fraction.

[4] In [4] and [6] it was mistakenly stated that M_2 was set to 1.0 TeV for Scan A. The actual value of M_2 used was 1.63 TeV in those papers.

[5] The corresponding Fig. 19(c) of [4] mistakenly showed the 99% CL exclusion contour.

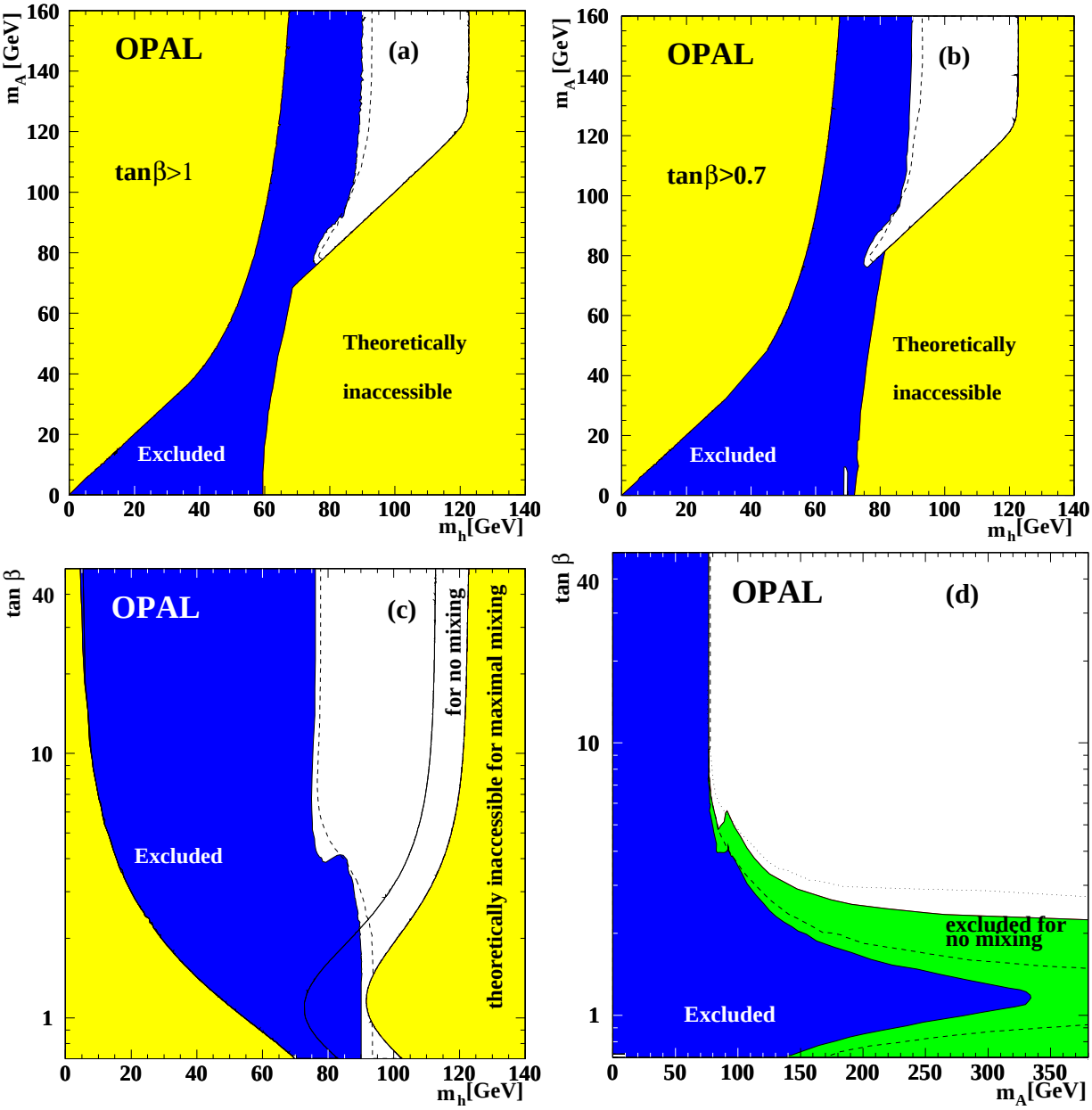

Fig. 14a–d. The MSSM exclusion for the "benchmark" scan described in the text of Sect. 6.2. Excluded regions are shown for **a** the (m_h, m_A) plane for $\tan\beta > 1$, **b** the (m_h, m_A) plane for $\tan\beta > 0.7$, **c** the (m_h, $\tan\beta$) plane, and **d** the (m_A, $\tan\beta$) plane. The black area is excluded at the 95% CL. The grey areas in **a**, **b** and **c** are theoretically inaccessible. In **b**, because of the wider permitted range of $\tan\beta$, more (m_h, m_A) points become available, and a small, unexcluded region appears at $m_\mathrm{h} \approx 70\,\mathrm{GeV}$, $m_\mathrm{A} < 10\,\mathrm{GeV}$ and $\tan\beta \approx 0.7$. This region can also be seen in **d**, although its projection in **c** is a small dot obscured by the $m_\mathrm{h} = 70\,\mathrm{GeV}$ tick mark. Shown in **d** is the excluded region for no scalar top mixing. In all figures, the black region is excluded for all values of the scalar top mixing. In **d**, the grey area is excluded for the case of no scalar top mixing. The dashed lines indicate the boundary of the region expected to be excluded at the 95% CL if only SM background processes are present. The dotted line in **d** is the expected limit for the case with no scalar top mixing.

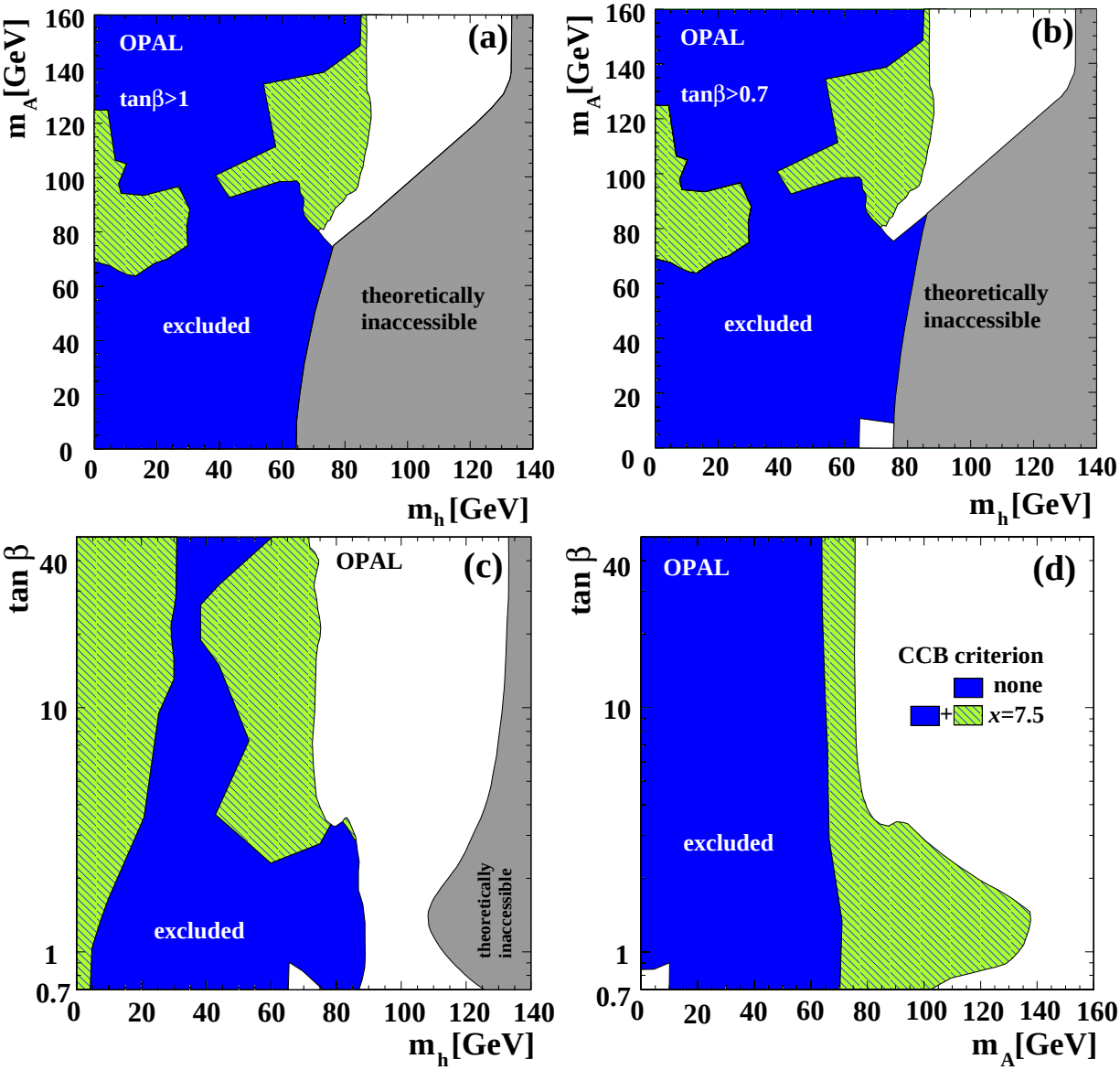

Fig. 15a–d. The MSSM exclusion for the general scan described in the text of Sect. 6.2. Excluded regions are shown for **a** the (m_h, m_A) plane for $\tan\beta > 1$, **b** the (m_h, m_A) plane for $\tan\beta > 0.7$, **c** the (m_h, $\tan\beta$) plane, and **d** the (m_A, $\tan\beta$) plane. All exclusion limits are at the 95% CL. The black areas are excluded without applying a CCB criterion (described in the text). The grey hatched areas are excluded when the CCB criterion is applied with $x = 7.5$. The grey areas in **a**, **b** and **c** are theoretically inaccessible.

In a more general scan (Scan C of [6]), all six parameters are varied independently within ranges motivated by theory, with the top quark mass taken at 165, 175 and 185 GeV, which allows for about $\pm 2\sigma$ of the current measurement error. The ranges for the parameters of this scan are $0 < m_0 < 1$ TeV, $0 < M_2 < 2$ TeV, $-2.5 \cdot m_0 < A < 2.5 \cdot m_0$, $-1 < \mu < 1$ TeV, $5 < m_\mathrm{A} < 2000\,\mathrm{GeV}$ and $0.7 < \tan\beta < 50$. For some parameter sets, the heavier CP-even Higgs boson (H^0) is light enough to be produced in the $\mathrm{H}^0\mathrm{Z}^0$ process, and in those cases the $\mathrm{h}^0\mathrm{Z}^0$ searches are considered sensitive to it, thereby extending the excluded area. Parameter sets giving rise to chargino or neutralino masses [41] or scalar top masses [42] already excluded by OPAL searches are considered excluded here. Models which give rise to large $\mathrm{Z}^0 \to \mathrm{h}^0\mathrm{Z}^*$ or $\mathrm{Z}^0 \to \mathrm{A}^0\mathrm{h}^0$ cross-sections incompatible with the measured Z^0 decay width (see [6]) are also considered excluded. The results for this scan are shown in Fig. 15. The dark area is excluded at the 95% CL. The unexcluded region for $m_\mathrm{h} \approx 70\,\mathrm{GeV}$ and $m_\mathrm{A} < 10\,\mathrm{GeV}$ has become larger in this more general scan, but it is still limited to the region of low $\tan\beta$.

For large values of A and μ, it is possible for the MSSM Lagrangian to have minima which have non-zero vacuum

expectation values for the $\tilde{t}$ fields which therefore break charge and colour symmetry [43]. Models with charge- and colour-breaking (CCB) global minima are inconsistent with the present state of the universe, and these may be identified [44] and not included in the model space considered here. Exceptions to this rule are models with local minima for which the tunneling rate to the global CCB minimum is small enough to allow the universe to remain in a non-CCB state throughout its estimated lifetime. A simple, approximate criterion to avoid CCB minima is [43]

$$A^2 + 3\mu^2 < x(m^2_{\tilde{t}_L} + m^2_{\tilde{t}_R}),$$

where $m_{\tilde{t}_L}$ and $m_{\tilde{t}_R}$ denote the left- and right-handed scalar top masses and $x \approx 3$. For a calculation [45] which includes the possibilities of false vacua which tunnel only slowly to CCB vacua, this condition is shown to be modified with $x \approx 7.5$. We show in Fig. 15 the regions in m_h, m_A and $\tan\beta$ in our general scan which we do not exclude but which lead to Lagrangians with CCB minima according to the looser criterion with $x = 7.5$. With this CCB criterion applied, absolute mass limits $m_A > 76.0$ GeV and $m_h > 72.2$ GeV are derived for $\tan\beta > 1$ at the 95% CL.

7 Conclusions

A search for neutral Higgs bosons has been performed based on the data collected at $\sqrt{s} \approx 189$ GeV with an integrated luminosity of approximately 170 pb^{-1}. Searches have been performed for the Standard Model process $e^+e^- \to H^0Z^0$ and the MSSM processes $e^+e^- \to h^0Z^0$, A^0h^0. The search channels are designed to detect $b\bar{b}$ and $\tau^+\tau^-$ decays of the Higgs bosons, and the process $h^0 \to A^0A^0$ is also considered. No significant excess of candidates is observed in the data beyond the expected Standard Model backgrounds, and we derive the following limits at the 95% confidence level. For the SM Higgs boson, we obtain a lower mass bound of 91.0 GeV. In the MSSM, we obtain the limits $m_h > 74.8$ GeV and $m_A > 76.5$ GeV assuming $\tan\beta > 1$, the mixing in the scalar top sector to be either zero or maximal, and the soft SUSY-breaking masses are 1 TeV. In the general scan of MSSM parameters, excluding parameter sets which result in Lagrangians with charge- and colour-breaking minima, we derive absolute mass limits of $m_h > 72.2$ GeV and $m_A > 76.0$ GeV for $\tan\beta > 1$ at the 95% confidence level.

Acknowledgements. We particularly wish to thank the SL Division for the efficient operation of the LEP accelerator at all energies and for their continuing close cooperation with our experimental group. We thank our colleagues from CEA, DAPNIA/SPP, CE-Saclay for their efforts over the years on the time-of-flight and trigger systems which we continue to use. In addition to the support staff at our own institutions we are pleased to acknowledge the Department of Energy, USA, National Science Foundation, USA, Particle Physics and Astronomy Research Council, UK, Natural Sciences and Engineering Research Council, Canada, Israel Science Foundation, administered by the Israel Academy of Science and Humanities, Minerva Gesellschaft, Benoziyo Center for High Energy Physics, Japanese Ministry of Education, Science and Culture (the Monbusho) and a grant under the Monbusho International Science Research Program, Japanese Society for the Promotion of Science (JSPS), German Israeli Bi-national Science Foundation (GIF), Bundesministerium für Bildung, Wissenschaft, Forschung und Technologie, Germany, National Research Council of Canada, Research Corporation, USA, Hungarian Foundation for Scientific Research, OTKA T-029328, T023793 and OTKA F-023259.

References

1. P.W. Higgs, Phys. Lett. **12** (1964) 132; F. Englert and R. Brout, Phys. Rev. Lett. **13** (1964) 321; G.S. Guralnik, C.R. Hagen, and T.W.B. Kibble, Phys. Rev. Lett. **13** (1964) 585.
2. S.L. Glashow, J. Iliopoulos, and L. Maiani, Phys. Rev. **D2** (1970) 1285; S. Weinberg, Phys. Rev. Lett. **19** (1967) 1264; A. Salam, *Elementary Particle Theory*, ed. N. Svartholm (Almquist and Wiksells, Stockholm, 1968), 367.
3. H.P. Nilles, Phys. Rep. **110** (1984) 1; H.E. Haber and G.L. Kane, Phys. Rep. **117** (1985) 75; R. Barbieri et al., *Z Physics at LEP1*, CERN 89-08, Vol. 2, 121; J.M. Frère and G.L. Kane, Nucl. Phys. **B223** (1983) 331; J. Ellis et al., Phys. Lett. **B123** (1983) 436; J. Ellis et al., Phys. Lett. **B127** (1983) 233.
4. OPAL Collaboration, G. Abbiendi et al., Eur. Phys. J. **C7** (1999) 407.
5. OPAL Collaboration, K. Ackerstaff et al., Eur. Phys. J. **C1** (1998) 425.
6. OPAL Collaboration, K. Ackerstaff et al., Eur. Phys. J. **C5** (1998) 19.
7. ALEPH Collaboration, R. Barate et al., Phys. Lett. **B440** (1998) 403; ALEPH Collaboration, R. Barate et al., Phys. Lett. **B440** (1998) 419; DELPHI Collaboration, P. Abreu et al., *Search for neutral Higgs bosons in* e^+e^- *collisions at* $\sqrt{s} = 183$ *GeV*, CERN-EP/99-06, accepted by Eur. Phys. J. **C**; L3 Collaboration, M. Acciarri et al., Phys. Lett. **B431** (1998) 437; L3 Collaboration, M. Acciarri et al., Phys. Lett. **B436** (1998) 389.
8. ALEPH, DELPHI, L3, and OPAL collaborations, and the LEP Working Group for Higgs Boson Searches, *Limits on Higgs Boson Masses from Combining the Data of the four LEP experiments at energies up to 183 GeV*, CERN-EP/99-060.
9. OPAL Collaboration, K. Ahmet et al., Nucl. Instr. and Meth. **A305** (1991) 275.
10. S. Anderson et al., Nucl. Instr. and Meth. **A403** (1998) 326.
11. OPAL Collaboration, K. Ackerstaff et al., *Search for Acoplanar Lepton Pair Events in* e^+e^- *Annihilation at* $\sqrt{s} = 161$, *172 and 183 GeV*, CERN-EP/98-122, submitted to Eur. Phys. J. **C**.
12. B.E. Anderson et al., IEEE Transactions on Nuclear Science **41** (1994) 845.
13. OPAL Collaboration, K. Ackerstaff et al., Phys. Lett. **B391** (1997) 221.
14. OPAL Collaboration, R. Akers et al., Phys. Lett. **B327** (1994) 397.

15. N. Brown and W.J. Stirling, Phys. Lett. **B252** (1990) 657; S. Bethke, Z. Kunszt, D. Soper and W.J. Stirling, Nucl. Phys. **B370** (1992) 310; S. Catani et al., Phys. Lett. **B269** (1991) 432; N. Brown and W.J. Stirling, Z. Phys. **C53** (1992) 629.
16. OPAL Collaboration, K. Ackerstaff et al., Eur. Phys. J. **C2** (1998) 213.
17. HZHA generator: P. Janot, *Physics at LEP2*, CERN 96-01, Vol.2, 309.
18. PYTHIA 5.721 and JETSET 7.408 generators: T. Sjöstrand, Comp. Phys. Comm. **82** (1994) 74; T. Sjöstrand, LU TP 95-20.
19. The grc4f 1.1 generator: J. Fujimoto et al., Comp. Phys. Comm. **100** (1997) 128. J. Fujimoto et al., *Physics at LEP2*, CERN 96-01, Vol.2, 30.
20. EXCALIBUR generator: F.A. Berends, R. Pittau, and R. Kleiss, Comp. Phys. Comm. **85** (1995) 437.
21. BHWIDE generator: S. Jadach, W. Płaczek, and B.F.L. Ward, *Physics at LEP2*, CERN 96-01, Vol.2, 286; UTHEP-95-1001.
22. KORALZ 4.0 generator: S. Jadach, B.F.L. Ward, and Z. Wąs, Comp. Phys. Comm. **79** (1994) 503.
23. PHOJET 1.05 generator: E. Budinov et al., *Physics at LEP2*, CERN 96-01, Vol.2, 216; R. Engel and J. Ranft, Phys. Rev. **D54** (1996) 4244.
24. G. Marchesini et al., Comp. Phys. Comm. **67** (1992) 465.
25. J.A.M. Vermaseren, Nucl. Phys. **B229** (1983) 347.
26. OPAL Collaboration, G. Alexander et al., Z. Phys **C69** (1996) 543.
27. J. Allison et al., Nucl. Instr. and Meth. **A317** (1992) 47.
28. OPAL Collaboration, K. Ackerstaff et al., Z. Phys. **C74** (1997) 1; OPAL Collaboration, R. Akers et al., Z. Phys. **C66** (1995) 19.
29. G. Hanson et al., Phys. Rev. Lett. **35**, 1609 (1975).
30. G. Parisi, Phys. Lett. **B74** (1978) 65; J.F. Donoghue, F.E. Low and S.Y. Pi, Phys. Rev. **D20** (1979) 2759.
31. OPAL Collaboration, M.Z. Akrawy et al., Z. Phys. **C49** (1991) 375.
32. JADE Collaboration, W. Bartel et al., Z. Phys. **C33** (1986) 23; JADE Collaboration, S. Bethke et al., Phys. Lett. **B213** (1988) 235.
33. OPAL Collaboration, K. Ackerstaff et al., Eur. Phys. J. **C2** (1998) 441.
34. ALEPH Collaboration, R. Barate et al., Phys. Lett. **B412** (1997) 173.
35. G. Fox and S. Wolfram, Nucl. Phys. **B149** (1979) 413.
36. OPAL Collaboration, R. Akers et al., Z. Phys. **C61** (1994) 209; DELPHI Collaboration, P. Abreu et al., Phys. Lett. **B347** (1995) 447.
37. R.D. Cousins and V.L. Highland, Nucl. Instr. and Meth. **A320** (1992) 331.
38. OPAL Collaboration, G. Alexander et al., Z. Phys. **C73** (1997) 189.
39. OPAL Collaboration, R. Akers et al., Z. Phys. **C64** (1994) 1.
40. OPAL Collaboration, M.Z. Akrawy et al., Z. Phys. **C49** (1991) 1.
41. OPAL Collaboration, G. Abbiendi et al., Eur. Phys. J. **C8** (1999) 255.
42. OPAL Collaboration, K. Ackerstaff et al., Z. Phys. **C75** (1997) 409.
43. J.M. Frère, D.R.T. Jones and S. Raby, Nucl. Phys. **B222** (1983) 11; L. Alvarez-Gaumé, J. Polchinski and M. Wise, Nucl. Phys. **B221** (1983) 495; J.P. Derendinger and C.A. Savoy, Nucl. Phys. **B237** (1984) 307; C. Kounnas, A.B. Lahanas, D.V. Nanopoulos and M. Quirós, Nucl. Phys. **B236** (1986) 438.
44. J.A. Casas, A. Lleyda and C. Muñoz, Nucl. Phys. **B471** (1996) 3; J.A. Casas and S. Dimopoulos, Phys. Lett. **B387** (1996) 107.
45. A. Kusenko, P. Langacker and G. Segre, Phys. Rev. **D54** (1996) 5824.